International Journal of Heat and Mass Transfer 272 (2027) 129604

Contents lists available at ScienceDirect

International Journal of Heat and Mass Transfer

journal homepage: www.elsevier.com/locate/ijhmt

Frosting and defrosting dynamics on slippery omniphobic covalently attached liquid coated microchannel heat exchangers

Jung Bin Yang [a,1], Siyan Yang [a,1], Donghyeon Yoo [b], Kaushik Chettiar [a], Zihao Liu [a], Sujan Dewanjee [a], Garrett Fleetwood [a], Omar Abdelhamid [a], Md Rakibul Hasan Roni [a], Seungyeon Lee [a,c], Cheng Zhang [d], Ali Riahi [d], Hyeonho Lee [e], Dong Rip Kim [e], Nenad Miljkovic [a,b,f,g,h,i,*]

[a] Department of Mechanical Science and Engineering, University of Illinois at Urbana-Champaign, Urbana, IL, USA
[b] International Institute for Carbon Neutral Energy Research (WPI-I2CNER), Kyushu University, 744 Motooka, Nishi-ku, Fukuoka, 819-0395, Japan
[c] Department of Mechanical Engineering, Seoul National University, Seoul, 08826, South Korea
[d] Rheem Manufacturing Company, Atlanta, GA, 30328, USA
[e] School of Mechanical Engineering, Hanyang University, Seoul, 04763, South Korea
[f] Materials Research Laboratory, University of Illinois at Urbana-Champaign, Urbana, IL, USA
[g] Department of Electrical and Computer Engineering, University of Illinois at Urbana-Champaign, Urbana, IL, USA
[h] Institute for Sustainability, Energy and Environment (iSEE), University of Illinois, Urbana, IL, USA
[i] Air Conditioning and Refrigeration Center, University of Illinois, Urbana, IL, USA

ARTICLE INFO

Keywords:
Frosting
Defrosting
Heat exchanger
Slippery surface
Anti-corrosion
SOCAL

ABSTRACT

Frost increases thermal resistance and air-side pressure drop, causes frequent defrosting, and thereby deteriorates overall system efficiency. Although slippery omniphobic covalently attached liquid (SOCAL) coatings have emerged as a promising lubricant-free liquid-like interface with potential anti-frosting functionality, their frosting performance on compact heat exchangers (HXs) has not yet been demonstrated. In this study, a SOCAL coating was applied to both aluminum coupons and aluminum louver-fin microchannel HXs using an SL1000 intermediate layer, and its frosting/defrosting characteristics were evaluated. Slippery interface of SL1000-SOCAL coatings broadened the droplet size distribution, increased inter-droplet spacing, and significantly suppressed ice-bridge and frost propagation, resulting in a frost-free duration of ~45–60 min, which was 4–6 times longer than that of bare aluminum coupons. The SL1000-SOCAL coating showed superior corrosion resistance and coating integrity, exhibiting no significant mass loss after 14 continuous days of the seawater acetic acid test. At the HX level, the SL1000-SOCAL-coated HX delayed heat-transfer degradation and extended the useful frosting time by 25.8–60.7% across the tested operating conditions. In a separate 3 h cyclic frosting/defrosting test, the mean number of required defrost events decreased from 6.7 ± 0.6 for the bare HX to 3.3 ± 0.6 for the SL1000-SOCAL HX. A generalized annual heating and economic analysis projects that the SL1000-SOCAL HX could reduce annual energy consumption by 270.9 kWh (12.7%) and annual heating cost by ~$40 for a representative 1.5 kW heating load. This work demonstrates that SOCAL coating is a promising strategy for improving frosting, defrosting, and corrosion characteristics of compact HXs.

1. Introduction

Frost formation on air-coupled heat exchangers (HXs) is a major challenge to low temperature thermal systems operating in cold and humid conditions [1–3]. For example, the recent push to electrify heating at the residential, commercial, and industrial scale requires the development of cold climate heat pumps that can extract heat from cold ambient air as low as −20°C [4–6]. Frosting on the evaporator of these systems presents a significant challenge to commercial and industrial adoption. Within the automotive sector, the move away from positive temperature coefficient (PTC) heaters towards heat pumps in electric vehicles (EVs) poses the same challenge [7,8]. Electric vehicles

* Corresponding author at: Department of Mechanical Science and Engineering, University of Illinois at Urbana-Champaign, Urbana, IL, USA.
E-mail address: nmiljkov@illinois.edu (N. Miljkovic).
[1] These authors contributed equally to this work as co-first authors.

https://doi.org/10.1016/j.ijheatmasstransfer.2026.129604
Received 31 May 2026; Received in revised form 23 August 2026; Accepted 18 September 2026
Available online 22 September 2026
0017-9310/© 2026 The Authors. Published by Elsevier Ltd. This is an open access article under the CC BY-NC-ND license (http://creativecommons.org/licenses/by-nc-nd/4.0/).

operating in cold climates exhibit significant range reduction, the need for frequent defrosting events or limited heat pump use, and hence limited market penetration for EVs at northern latitudes [9].

As frost accumulates on the fins of an HX, it increases thermal resistance, blocks air passages, raises pressure drop, and necessitates periodic defrosting, thereby reducing heat-transfer capacity and overall system efficiency [3,10–12]. This problem is particularly critical for louver-fin or fin-tube HXs, where narrow air passages can be readily obstructed by frost, leading to rapid deterioration of air-side performance [13–15]. For example, in air-source heat pumps, frost accumulation has been reported to decrease heating capacity by 30–57% and coefficient of performance (COP) by 35–60% [16], while field measurements under mal-defrost conditions showed heating capacity and COP losses of up to 40.4% and 43.4% [17], respectively. For these reasons, practical anti-frosting strategies are increasingly important for heat transfer devices, such as refrigeration units and building heat pumps.

Researchers have sought to improve frosting and defrosting performance through various approaches [18–21]. Liang et al. [18] analyzed the condensation, frosting, and defrosting on the surface of a single straight fin under constrained airflow conditions. They observed a W-shaped frost distribution caused by the edge effect. The average frost thickness at the windward reinforcement rib was 38.5% lower than that at the fin edge. During defrosting, the maximum rate of reduction in frost-covered area reached 10.21 mm^2/s. These findings provide guidelines for optimizing fin geometry and inducing more uniform frost formation and defrosting behavior. Wei et al. [20] verified the heating performance of an air source heat pump with vapor injection (ASHPVI) under frosting conditions. Their ASHPVI, constructed in a constant-temperature and humidity laboratory, improved heating capacity by 11.31% even under frost-formation conditions, but lowered the coil surface temperature by up to 4.6°C, thereby accelerating frost formation. The authors suggested that ASHPVI, which does not apply vapor injection under frosting conditions, would be more advantageous for improving heating performance.

Recently, surface modification has attracted attention with passive anti-frosting approaches, which do not require additional power input or complicated control [2,22,23]. Superhydrophobic (SHP) coatings are attracting many researchers because their low surface energy and low contact angle hysteresis (CAH) prevent frost nucleation and promote rapid droplet shedding [24–26]. For example, Boyina et al. [24] reported that meter-scale finned HXs with SHP coating reduced frost accumulation and delayed performance degradation (until half of maximum capacity) by 3 times. Also, they reduced defrost time and energy consumption by 50% and lowered the retained water by 75% relative to uncoated and superhydrophilic counterparts. Yang et al. [25] demonstrated that SHP HX performance depends strongly on fin geometry. Specifically, for a 1 mm fin spacing, water bridges readily formed and even reduced heat transfer, whereas for a 3 mm spacing, the SHP HX exhibited a 14% lower steady-state pressure drop because droplets could more readily slip or jump off the fins.

In addition to SHP, slippery liquid-infused porous surfaces (SLIPS) have also been investigated because of their ‘SHP-like’ behavior due to their lubricant-mediated interface, minimizing contact line pinning, reducing CAH, and suppressing frost propagation. Seo et al. [27] reported that the lubricant generated an attractive force between condensates and mediates active droplet coalescence. Enhanced droplet coalescence by a lubricant layer reduces frost propagation, thereby achieving excellent anti-frosting performance. Similarly, Jiang et al. [28] reported that the high droplet mobility of SLIPS accelerates droplet coalescence. Furthermore, the increased inter-droplet distance resulting from this coalescence induces local freezing, rather than directional frosting propagation via ice bridges, thereby potentially reducing the rate of frost propagation. Although these studies established SLIPS as a promising anti-frosting platform, their translation and evaluation in real compact HXs remains limited. Available device-level studies are concentrated more on feasibility or condensation retention behavior than on sustained frosting/defrosting operation [29,30]. This is because frost growth can induce lubricant depletion through dendrite-driven capillary forces [31], a phenomenon attributed to the inherent instability of the mobile lubricant layer.

Recently, slippery omniphobic covalently attached liquid (SOCAL) coatings have emerged as a lubricant-free liquid-like alternative to SLIPS. Wang and McCarthy first introduced 'instant' realization of SOCAL [32], formed by acid-catalyzed graft polycondensation of dimethyldimethoxysilane, producing surfaces that are stable under pressure and durable at elevated temperatures. In subsequent studies, researchers highlighted that these liquid-like layers exhibit ultralow CAH [32–34], have high droplet mobility [35,36], and show resistance to frosting and fouling [37,38], while avoiding lubricant depletion that constrains conventional SLIPS [39,40]. Zhang et al. [37] demonstrated that the polymer mobile chain (quasi-liquid surface, 26.1 kPa) exhibits a lower ice adhesion force than bare glass (275.8 kPa). Sarma et al. [41] also reported a sustainable, low-ice-adhesion force (14 kPa) arising from a quasi-liquid/ice interface with an ultralow shear modulus that remained effective after chemical rinsing, heating, water impingement, and wiping. However, these studies showed indirect anti-frosting performance using ice-adhesion force measurements rather than a frosting test under airflow. Also, these tests were conducted on coupon-level samples rather than coatings applied to air-coupled HXs. Ghaddar et al. [30] applied the quasi-liquid coating to commercial HXs, but they compared water retention only under condensation conditions, not frosting. To the best of our knowledge, direct frosting experiments on SOCAL-coated compact HXs have not yet been reported.

In this study, we apply a SOCAL coating to an aluminum louver-fin microchannel HX and evaluate its anti-frosting performance, ranging from coupon-level interfacial behavior to full HX operation. The novelties of this work lie in three main aspects. First, to the best of our knowledge, this study provides the first direct evaluation of frosting and defrosting on a SOCAL-coated compact louver-fin microchannel HX under forced-convection conditions. Second, the study establishes a multiscale experimental framework by combining coupon-level measurements of droplet coalescence, inter-droplet spacing, ice-bridge propagation, macroscopic frost spreading, and anti-frosting duration with HX-level measurements of heat-transfer-rate degradation, air-side pressure-drop growth, and cyclic frosting/defrosting behavior. Finally, the study evaluates not only anti-frosting performance and defrosting performance but also corrosion resistance, coating integrity, and cyclic durability.

To substantiate these advances, the morphology, thickness, chemical composition, and wettability of bare, SL1000, and SL1000-SOCAL surfaces are characterized. Coupon-level experiments are then used to identify the intrinsic condensation and ice-bridging behaviors of the SOCAL interface, while identical bare and SL1000-SOCAL-coated HXs are compared under multiple inlet air velocities and coolant temperatures. Corrosion resistance and coating integrity are systematically assessed through potentiodynamic polarization, seawater acetic acid testing, and Cu-electrodeposition-based defect quantification. In addition, 3 h cyclic frosting/defrosting tests and an accelerated 50-cycle durability assessment are conducted to evaluate meltwater removal, re-frosting performance recovery, and possible early-stage coating degradation. The SL1000-SOCAL HX extends the useful frosting time by 25.8–60.7% across the tested operating conditions, decreases the mean number of required defrost events from (6.7 ± 0.6) to (3.3 ± 0.6) during the 3 h cyclic test, and retains comparable anti-frosting performance after 50 frosting/defrosting cycles without observable cracking or large-area delamination. By integrating interfacial frosting mechanisms, HX-level thermal-hydraulic performance, corrosion protection, and cyclic durability within a single framework, this work demonstrates the engineering potential of lubricant-free SOCAL coatings for compact air-side HX applications.

2. Experimental

2.1. Heat exchanger geometry

Aluminum louver-fin microchannel HXs were used for the HX-level frosting experiments. The HX consisted of multiport flat tubes connected to round headers, with louvered fins inserted between adjacent tubes. The overall core dimensions are denoted by HX length, L_{HX}, and height, H_{HX}. The characteristic geometric parameters of the microchannel core, including the diameter of headers (D_h), tube height (H_t), tube pitch (p_t), fin pitch (p_f), tube width (W_t), and fin width (W_f), are defined schematically in Fig. 1, and their specific values are summarized in Table 1. For the HX-level frosting experiments, an uncoated bare HX and a SOCAL-coated HX having the same geometry were compared. Flat aluminum coupons were additionally used for coupon-scale characterization and frosting performance quantifications to isolate the interfacial frosting behavior from the geometric complexity of the full HX.

2.2. Sample preparation

Aluminum (88685K12, Al1100, McMaster-Carr) coupon substrates (50 mm × 50 mm × 1.6 mm) were used for coupon-level anti-frosting performance evaluation and surface characterization. Prior to coating, the coupons were sequentially cleaned with acetone (CAS 67-64-1, Fisher Chemical), ethanol (CAS 64-17-5, Decon Labs, Inc.), and deionized (DI) water (CAS 7732-18-5, Aqua Solutions, Inc.). To achieve a SOCAL coating on the Al surface, a hydrogenated amorphous silicon (a-Si:H, SL1000, SilcoTek) intermediate layer was applied. This layer was deposited via chemical vapor deposition (CVD), yielding a chemically robust, multilayered Si-based coating on the samples. It should be noted that, in many studies, these Si-based coatings have been adopted as intermediate layers to achieve SOCAL coatings due to their high hydroxyl group density and affinity with silane coupling agents [34,42,43]. Subsequently, the SOCAL coating was applied according to the recipe proposed by Wang and McCarthy [32]. The method they employed utilizes sulfuric acid as a catalyst and water molecules as co-monomers to "instantly" graft a PDMS brush (SOCAL polymer brush) onto the surface. To prepare the SOCAL solution, 100 g of isopropanol (CAS 67-63-0, Sigma Aldrich), 20 g of dimethoxydimethylsilane (CAS 1112-39-6, Sigma Aldrich), and 1 g of sulfuric acid (H_2SO_4, CAS 7664-93-9, Sigma Aldrich) were mixed. The solution was stirred at 800 rpm for 30 min using a magnetic stirrer, then allowed to stabilize for 30 min before use. The SL1000-coated aluminum substrates were immersed in the SOCAL solution, withdrawn, and allowed to dry vertically in ambient air. It should be noted that because the SOCAL (PDMS) brush polymerizes with water molecules in the air, the SOCAL coating is grafted onto the surface during drying, rather than while immersed in the solution [32]. The SL1000-coated and bare Al samples were used as control groups alongside the SOCAL-coated samples.

Table 1
Specifications of the louver-fin heat exchanger (HX) used for frosting experiments.

Specification	Values	Specification	Values
HX length (L_{HX})	139 mm	HX height (H_{HX})	130 mm
Diameter of headers (D_h)	20 mm	Microchannels per tube	16
Tube/Fin width (W_t/W_f)	16 mm	Number of tubes (first/second pass)	13 (6/7)
Tube pitch (p_t)	9.4 mm	Tube height (H_t)	1.3 mm
Fin pitch (p_f)	1.6 mm	Heat transfer area	0.2497 m^2

For the HX-level frosting experiments, aluminum louver-fin microchannel HXs (MCHE LX-C2479, Midea) were prepared using identical processes to those used for the coupon-level samples. Since the SL1000 coating employs a non-line-of-sight CVD method, and the SOCAL coating utilizes a solution-based dip-coating technique, both were deposited uniformly across the louver-fin microchannel HXs, despite their geometrical complexity. The anti-frosting performance of the SOCAL-coated HX was evaluated using a bare HX as a control group.

2.3. Surface characterization of coupon-level samples

The surface morphology of the bare, SL1000, and SL1000-SOCAL surfaces was characterized using a scanning electron microscope (SEM, JSM-7000F, JEOL). To measure the thickness, SEM images of cross-sectional tilted view were compared using a focused ion beam (FIB, Scios, FEI) milling process. The chemical composition and bonding were characterized using X-ray photoelectron spectroscopy (XPS, AXIS Supra+, Kratos Analytical). The static contact angle (CA), advancing CA, and receding CA of each sample were measured using a contact angle goniometer (Model 250, Ramé-Hart Instrument Co.). Reported values were obtained from at least 5 independent samples with a water droplet volume of 10 μL.

To evaluate coating corrosion resistance and integrity, three different quantitative experiments were conducted:

(1) Potentiodynamic polarization test: the electrochemical corrosion behavior was measured using a potentiostat (Reference 600+, Gamry Instruments). Specifically, a three-electrode cell configuration was employed, consisting of the coupon samples as the working electrode, an Ag/AgCl (Saturated KCl) electrode as the reference electrode, and graphite as the counter electrode. The electrolyte was a 0.5 M aqueous NaCl solution, and each coupon was stabilized by being held at open-circuit potential (OCP) for at least 16 h. Subsequently, polarization curves were measured over a potential range of ±0.3 V relative to the OCP, with a scan rate of 1 mV/s. It should be noted that masking tape was applied to

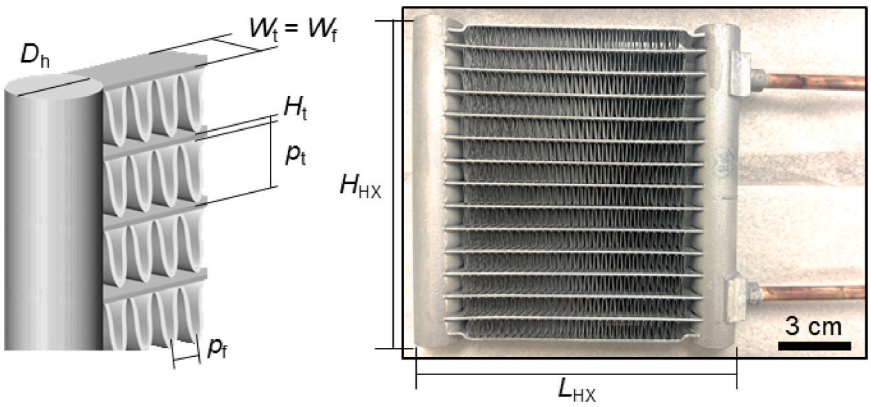

Fig. 1. Schematic and photograph illustrating the geometry of heat exchanger (HX) samples. Schematic not to scale.

the samples to ensure that only a 1 cm^2 surface area was exposed to the electrolyte, thereby facilitating the comparison of corrosion current densities and minimizing edge effects.

(2) Sea water acetic acid test (SWAAT): The SWAAT was conducted in a cyclic corrosion test chamber (Q-fog CRH-600, Q-Labs) in accordance with ASTM G85 Annex A3. To prepare the synthetic seawater, we mixed 42 g/L of sea salt (SS15–10, Instant Ocean) into DI water. Subsequently, 10 mL of acetic acid (CAS 64-19-7, Sigma Aldrich) was added per liter of the mixture, and the pH was adjusted to 2.8–3.0 using sodium hydroxide (CAS 1310-73-2, Sigma Aldrich). The samples were sprayed with the mixture inside the chamber for 30 min at 49°C, followed by a 90 min incubation period at 49°C and 98% relative humidity (RH). This 2 h cycle was repeated for 14 days. For quantification, the mass loss (using a precise scale, ENTRIS224I-1SUS, Sartorius Lab Instruments, resolution of 0.1 mg) due to corrosion per unit area was determined by dividing the mass difference before and after the SWAAT by the surface area. Reported values were obtained from at least 3 independent samples.

(3) Surface defect quantification: because pinhole-type discontinuities can serve as preferential sites for localized corrosion initiation, the surface defect density was quantified as an indicator of coating integrity. To visualize these defects, we utilized the preferential deposition of Cu. Since Al substrate is exposed to the electrolyte and electric field only at these discontinuities, Cu can selectively deposit on its defect region during electrodeposition. Specifically, 1 M H_2SO_4 and 0.2 M $CuSO_4{\cdot}5H_2O$ (CAS 7758-99-8, Fisher Chemical) were used as the plating solution, and a 99.9% pure Cu sheet (8963K139, McMaster-Carr) was used as the anode. To ensure uniform deposition, the distance between the anode and the cathode (samples) was maintained within 2 cm, and the solution was gently stirred with a magnetic stirrer. The temperature of the plating solution was maintained at room temperature by storing the whole bath inside a temperature-controlled silicone oil bucket. To ensure uniform deposition, the pulse current (current density of 100 mA/cm^2) was applied for 1 s on and 4 s off for a total of 30 min. An optical microscope (optical mode in 3D laser scanning confocal microscope, VK-X1000, Keyence) was used to quantify the surface defect at a fixed magnification. The resulting Cu islands marked the locations of pinhole defects, and the pinhole density was determined by normalizing the number of Cu deposits by the analyzed surface area. It should be noted that there are particulate-like structures in pristine SL1000 and SL1000-SOCAL, which are presumed to result from aggregation during the SL1000 CVD process; therefore, color optical images are used to distinguish the Cu-plated spots, and the size of the captured image was 211.73×282.40 μm^2. A total of 10 independent measurements were analyzed and averaged.

2.4. Coupon-level frosting experiments

Coupon-level frosting experiments were conducted, as described in the previous report [44]. Specifically, it was performed under quiescent ambient conditions in a temperature- and humidity-controlled laboratory, where the air temperature was maintained at 20 ± 2°C and the RH was controlled at 45–50%. The local RH near the sample was monitored using a humidity probe (HX93BDV0, Omega). Flat coupon samples were mounted horizontally on a temperature-controlled Peltier cooling stage (TP104SC-mk2000A, Instec). Each sample was initially equilibrated at room temperature and then cooled to the target substrate temperature of −10°C at a rate of 30 °C/min. During the test, the cooling stage was operated with coolant supplied at approximately −2°C to maintain a stable low-temperature condition using a chiller (6160T21A130DDNT, PolyScience). To isolate the intrinsic condensation-frosting behavior of the coupon-level samples, all tests were performed under static conditions without any external airflow. These quiescent experiments were designed to identify the intrinsic surface-mediated condensation and ice-bridging mechanisms rather than to reproduce the aerodynamic conditions within the HX. Accordingly, the measured droplet spacing and ice-bridge propagation velocities are not directly extrapolated to the forced-convection HX experiments. The schematic illustration of the coupon-level frosting test setup is shown in Fig. 2. The time-resolved evolution of condensation, freezing, and subsequent frost growth was recorded in the top-view using an upright optical microscope (Eclipse LV100, Nikon) equipped with a digital single-lens reflex (DSLR) camera (DS-Qi2, Nikon). For events requiring higher temporal resolution, such as rapid ice-bridge formation, the DSLR camera was replaced with a high-speed camera (Phantom V711). For macroscale frost-propagation measurements, the field of view was widened to capture the entire coupon surface, and image acquisition was continued until the observable area was completely covered by frost. Unless otherwise noted, the anti-frosting duration was defined as the elapsed time from the moment the sample reached the target substrate temperature to complete frost coverage of the observable coupon area. The recorded image sequences were analyzed to quantify the frosting initiation and end. Frosting onset was defined as the first observable droplet freezing event. The droplet size at frosting onset was measured using the equivalent projected droplet diameter, and the corresponding inter-droplet spacing was defined as the edge-to-edge distance between neighboring droplets immediately before ice bridging occurred. The ice bridging speed was determined from the displacement of the advancing bridge tip over time, while the apparent frosting speed was obtained from the temporal increase in the projected frosted area on the coupon samples.

2.5. Heat-exchanger-level open-loop wind tunnel frosting experiments

Heat exchanger frosting experiments were performed using a custom-built facility consisting of an open-loop wind tunnel with a closed-loop coolant side, as schematically shown in Fig. 3. The microchannel HX samples were mounted vertically in the test section of the acrylic square duct (139.7×139.7 mm^2). A centrifugal fan (Twin city fan & blower Co.) located downstream of the test section drew ambient air through the inlet, a flow straightener, and the HX sample, thereby establishing a controlled forced-convection flow over the air-side surface of the microchannel HX. The air inlet temperature and outlet temperature were monitored using thermocouples (type K) positioned upstream and downstream of the test section, respectively. The inlet humidity sensor (THD-DD1-C, Autonics) was placed near the HX entrance. The air-side inlet temperature and humidity were well

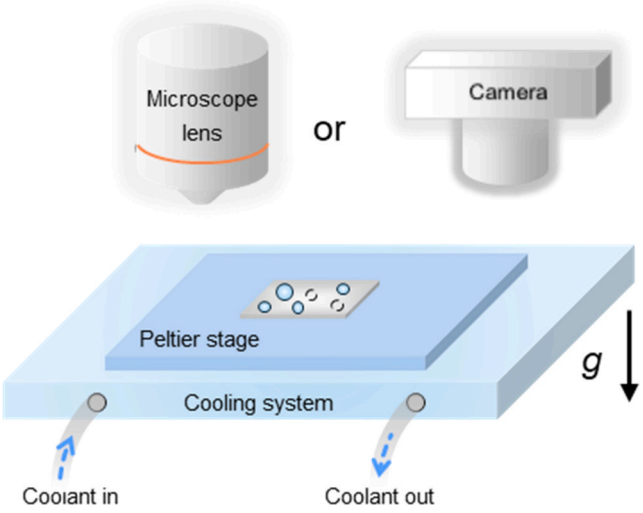

Fig. 2. Schematic illustration of coupon-level frosting experiment. Schematic not to scale.

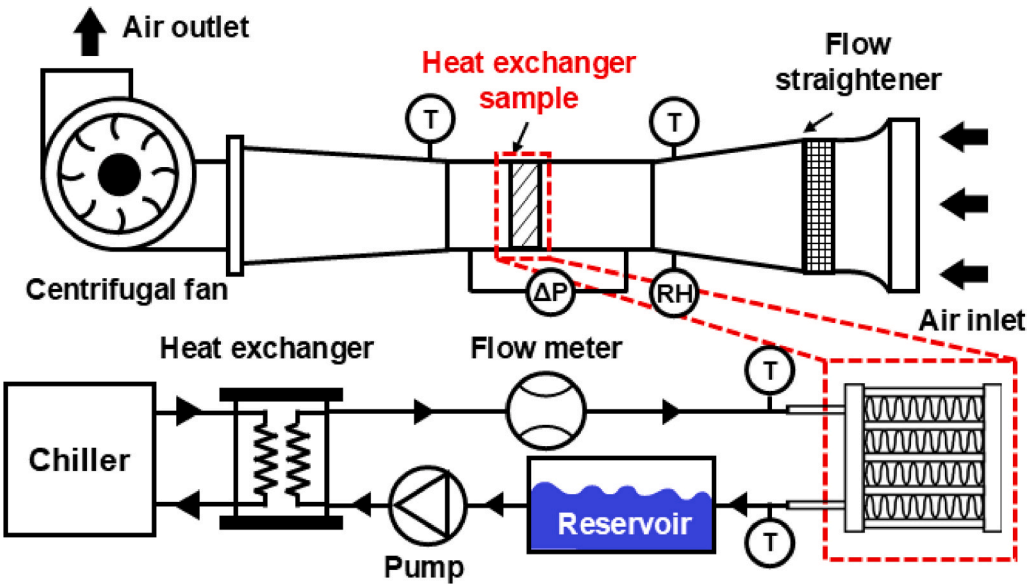

Fig. 3. Schematic of the experimental setup of the open-loop wind tunnel facility used to characterize the HX-level frosting test. Schematic not to scale.

maintained as constant conditions in the laboratory. A humidifier (HQ-4H-JS905, PuDina) and dehumidifier (TP70WK, Honeywell) were utilized to control RH more precisely between 45% and 50%. As a result, the air temperature and RH were measured as 20.5 ± 0.6°C and 47.2 ± 2.9%, respectively, across all test conditions. The air-side pressure drop across the HX was measured using a differential pressure transducer (264 Series, Setra systems Inc.) connected between the upstream and downstream sides of the HX sample. The inlet air velocity was controlled by adjusting the fan speed and the hot-wire anemometer (HHF-SD1, Omega) before the test.

On the coolant side, the HX was connected to a recirculating liquid loop consisting of a reservoir, gear pump (GB-P35, Micropump), a magnetic flow meter (DMA150AAACA1, Endress+Hauser), and a brazed plate HX (GB200H-10, GEA PHE Systems) coupled to a chiller (6762T41A130DDNT, PolyScience). The coolant temperature supplied to the microchannel HX was controlled through the chiller-side loop, while the coolant flow rate in the primary loop was maintained at 2.5 L/min. The HX inlet and outlet coolant temperatures were measured using resistance temperature detectors (RTD, Reotemp Pt 385, Class A) installed right before and after the ports. Prior to each run, the chiller was turned on for 30 min to reach the steady-state coolant temperature. A frosting experiment was initiated by exposing the air-side of the HX to the humid air flow while circulating subcooled coolant through the HX internal channels. Each experiment was continued until severe frosting developed on the air-side surface, corresponding to 70% of the heat transfer rate of its initial value. The initial heat transfer rate was defined as the point at which the heat transfer rate stabilized, with variations remaining below 1%. After each test, the HX was uninstalled, dried using a nitrogen gas blower, and completely dried for 24 h. The heat transfer rate ($\dot{Q}$) of the HX was calculated from the coolant-side energy balance as:

$$\dot{Q} = \dot{m}_c c_{p,c} \times (T_{HX,out} - T_{HX,in})$$

where $\dot{m}_c$ is the coolant mass flow rate (kg/s), $c_{p,c}$ is the specific heat of coolant (J/kg·K), and $T_{HX,in}$ and $T_{HX,out}$ are the coolant temperature (K) of HX inlet and outlet, respectively. The operating coolant was prepared by mixing DI water and ethylene glycol (107-21-1, Fisher Chemical) in a 1:1 ratio, and its density and specific heat were calculated from the previous literature [45].

As a parameter study, the inlet air velocity and coolant temperature were varied while keeping the remaining operating conditions constant.

Table 2
Experimental conditions.

Test condition	Air-side			Coolant-side	
	Inlet air temperature	Inlet air RH	Inlet air velocity	HX inlet temperature	Flow rate
C1	20.5°C	47.2%	1 m/s	−5°C	2.5 L/min
C2	20.5°C	47.2%	2 m/s	−5°C	2.5 L/min
C3	20.5°C	47.2%	3 m/s	−5°C	2.5 L/min
C4	20.5°C	47.2%	2 m/s	−7°C	2.5 L/min
C5	20.5°C	47.2%	0.5 m/s	−7°C	2.5 L/min

Table 2 presents the various test conditions conducted in this research. Using C2 in Table 2 (air velocity of 2 m/s, HX inlet temperature of −5°C) as the baseline, the influence of each factor was analyzed by varying the air velocity and coolant temperature conditions one at a time. In the case of a 3 h cyclic frosting/defrosting test, the pump for the coolant entering the HX was turned off and remained off for 6 min for defrosting. Bare and SL1000-SOCAL-coated HX having identical geometries were tested under the same conditions, and each condition was repeated 3 times. To evaluate possible degradation induced by repeated frosting/defrosting, the SL1000-SOCAL HX underwent an accelerated 50-cycle frosting/defrosting test using C5 condition in Table 2 (air velocity of 0.5 m/s, HX inlet temperature of −7°C). The lower HX inlet temperature increased the thermodynamic driving force for frost formation, while the reduced air velocity limited shear-assisted condensate removal, enabling rapid and repeatable frosting/defrosting cycling. This sequence was repeated consecutively for 50 cycles over approximately 7 h. After completing the cyclic exposure, the same HX was retested three times under the baseline C2 condition, and its useful frosting time was compared with the pre-cycling C2 results. Specific experimental conditions, measurement accuracies, and maximum calculation uncertainties of the experiment are shown in Tables 2 and 3, respectively. The uncertainty of the calculated heat transfer rate was evaluated, following the previous report [30].

2.6. Annual heating performance and economic analysis

To effectively evaluate the long-term system-level impact of the HX coatings, a generalized heat pump cycle simulation was applied to the continuous wind-tunnel experimental data. For the economic analysis, the frosting heat transfer performance was averaged across three independent 3-hour cyclic frosting/defrosting experiments (C2) for both the

Table 3
Measurement accuracies of the experimental measurements and calculated values.

Parameters (Instrument)	Measurement accuracy and maximum calculation uncertainty
Air temperature (Thermocouple, Type K)	±0.15°C
Coolant temperature (RTD)	±0.1°C
Coolant flow rate (Magnetic flow meter)	±0.8%
Air flow rate (Anemometer)	±5%
Humidity (RH sensor)	±3%
Pressure drop (Differential pressure transducer)	±1%
Heat transfer rate	±74.2 W

bare and SL1000-SOCAL HXs. Because the wind-tunnel tests were conducted using an ethylene glycol/water loop without an active compressor, the compressor power consumption (W_{cp}) was estimated using a standardized linear correlation derived from our prior full-system experimental testing [46]. Based on these experimental observations, the compressor power (in Watts) is modeled as a function of the real-time evaporator cooling capacity (Q_{refr} in Watts):

$$W_{cp} = 0.2Q_{refr} + 500$$

The correlation is used here as a first-order representation of compressor power rather than as a detailed compressor model. Examination of the underlying full-system experimental data revealed an approximately linear relationship between compressor power and evaporator capacity over the primary active-heating range, with greater deviations at very low loads. Because the objective of the present analysis is to compare the relative system-level consequences of the bare and coated HXs, the same empirical correlation was applied consistently to both cases. Accordingly, the resulting energy and economic estimates should be interpreted as comparative projections rather than absolute predictions of heat-pump performance. During the experimentally observed natural-defrost periods ($Q_{refr} < 5$ W), the simulated compressor power was set to zero, and the 1500 W heating demand was supplied by the auxiliary heater. This represents a simplified heating-interruption assumption rather than a model of reverse-cycle defrost. Actual heat-pump systems may employ compressor shutdown, reduced-capacity operation, or reverse-cycle defrost; quantifying these effects requires system-level testing and is outside the scope of the present study.

To simulate real-world residential heating demands, a constant target room heating load of 1500 W was established. The total heat delivered by the heat pump cycle (Q_{heat}) is calculated as the sum of the evaporator load (heat absorbed from the outside air) and the compressor work (the electrical work done by the compressor that is inherently transferred to the refrigerant):

$$Q_{heat} = Q_{refr} + W_{cp}$$

Whenever the system heat output dropped below the 1500 W target, a simulated auxiliary positive temperature coefficient (PTC) electrical heater was activated to cover the exact shortfall:

$$PTC = 1500 - Q_{heat}$$

The total electrical power consumed by the system is the sum of the compressor work and the PTC backup power. Finally, the effective system coefficient of performance (COP) is calculated by dividing the target room demand by the total electrical power consumed.

Annual energy consumption was projected using the Department of Energy (DOE) and Air-conditioning, Heating, and Refrigeration Institute (AHRI) 210/240 standard guidelines [47]. The analysis assumes an operation of 1701 heating load hours, which represents the updated standard for DOE/AHRI Climate Region IV (*e.g.*, Illinois) to reflect modern building envelopes. Electricity costs were calculated at a flat rate of $0.15 per kWh.

To ensure an accurate comparison of steady-state performance, the initial transient cycles of the experiments were discarded. Observation of the continuous data revealed differing stabilization periods for the two surfaces. (1) Bare HX: The uncoated baseline exhibited a progressive decline in cooling capacity over the first three cycles as initial frost embedded into the coil. The performance only stabilized into a predictable pattern starting from the fourth cycle. Therefore, to capture the true, long-term fouled state of the Bare coil, averages were calculated utilizing the 4th cycle and onward. (2) SL1000-SOCAL HX: The coated coil demonstrated rapid stabilization, mitigating the progressive capacity degradation seen in the Bare coil. Consequently, stable averages for the SOCAL surface were reliably calculated starting from the 2nd cycle onward.

3. Results and discussion

3.1. Surface morphologies, chemistry, and wettability of SL1000-SOCAL surfaces

Fig. 4 compares the surface morphology, thickness, chemical bonding and composition, and wettability of the bare Al, SL1000, and SL1000-SOCAL surfaces. As shown in the top-view SEM images in Fig. 4a, the bare Al surface exhibits microscale roughness originating from the native metal substrate and rolling lines during processing. After deposition of the SL1000 layer, the amorphous Si layer filled the microgrooves of the Al surface, resulting in a smoother topography. Following the application of the SOCAL coating, the surface retains comparable smoothness to that of SL1000, and there appears to be no significant difference in apparent roughness visually compared in the SEM image. However, according to the previous literature [33], SOCAL polymer brushes (here, PDMS) cover surface defects, thereby imparting self-smoothing characteristics to the surfaces. This property ensures that the SL1000-SOCAL surface does not exhibit high-roughness-dependent hydrophobicity and low CAH, but rather exhibits slippery, liquid-like characteristics designed to minimize contact line pinning. The cross-sectional tilted-view SEM images in Fig. 4b further confirm the coating interface and its thickness. Both SL1000 and SL1000-SOCAL samples exhibit a conformal intermediate layer with thicknesses of ~1.01 ± 0.2 μm and ~1.03 ± 0.1 μm, respectively. It should be noted that there is no significant difference in thickness between the two coatings, as the SOCAL coating consists of a thin (~10 nm) polymer brush covalently bonded to the surface [32].

On the other hand, XPS analysis revealed C, O, and Si peaks for both SL1000 and SL1000-SOCAL coatings, and Fig. 4c shows the Si 2p XPS narrow spectra of both coatings. For the SL1000 surface, peaks centered at 99.3 and 103.4 eV are assigned to a-Si [48] and SiO_2 [49], respectively, confirming the Si-based nature of the intermediate layer. After the SOCAL coating process, a new peak appears at 102 eV, corresponding to C_2-Si-O_2 [49], together with the SiO_2 peak. The emergence of this siloxane-related peak indicates the successful formation of a PDMS brush (SOCAL) layer on the SL1000 intermediate layer. These results are consistent with the intended coating architecture, in which the SL1000 underlayer provides a suitable platform for subsequent SOCAL grafting.

The wettability results in Fig. 4d show that the SOCAL treatment markedly altered the surface static and dynamic wetting behavior. The bare Al surface exhibits a CA of 87.6 ± 1.7° and a CAH of 34.9 ± 5.9°. The SL1000 surface shows hydrophilic characteristics, as CA and CAH exhibit 43.9 ± 6.5° and 36.0 ± 1.8°, respectively. In contrast, the SL1000-SOCAL surface maintains a high CA (103.7 ± 2.4°) but low CAH (2.3 ± 1.3°), which demonstrates that the SOCAL coating has slippery characteristics and has a lower friction force with the water droplet on its surface. Taken together, smooth morphology, siloxane-based surface

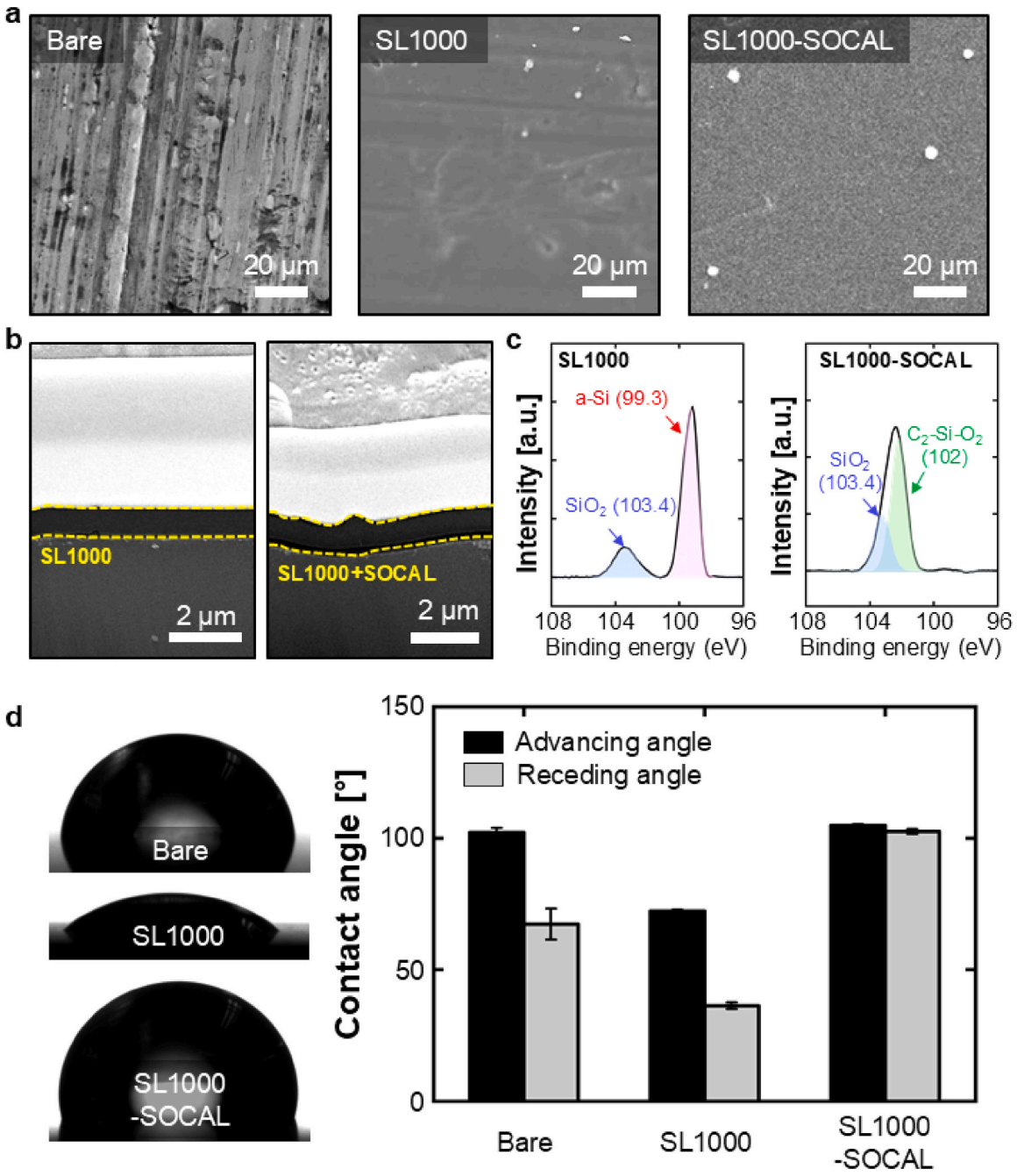

Fig. 4. Surface characteristics, including morphology, surface chemistries, and wettability. (a) Top-view scanning electron microscope (SEM) images of bare, SL1000, and SL1000-SOCAL surfaces. (b) Cross-sectional tilted-view SEM images of SL1000 and SL1000-SOCAL surface. (c) Si 2p X-ray photoelectron spectroscopy (XPS) narrow peak of SL1000 and SL1000-SOCAL surfaces. (d) Photographs of static contact angle (CA) and a graph of advancing and receding CA of bare, SL1000, and SL1000-SOCAL surfaces.

chemistry, and ultralow CAH confirm the successful fabrication of the SL1000-SOCAL coating and explain its expected advantage for promoting condensate mobility and suppressing ice-bridge-mediated frost propagation in the subsequent frosting experiments.

3.2. *Anti-frosting performance of coupon-level SL1000-SOCAL samples*

Since microscale condensation and freezing dynamics directly govern macroscopic frosting behavior, we first systematically characterized droplet condensation dynamics (Fig. 5). For clarity of presentation and to facilitate the physical discussion, the subsequent results are presented in the order of increasing CA: SL1000-coated, bare, and SL1000-SOCAL coated samples in Figs. 5–7. The results reveal that, compared with bare and SL1000 surfaces, the SL1000-SOCAL surface exhibits two distinct differences during the condensation stage. First, in terms of droplet coalescence dynamics, the SL1000-SOCAL surface differs markedly from the other two surfaces. On the bare and SL1000 surfaces, adjacent condensate droplets grow until their three-phase contact lines come into contact, triggering coalescence driven by surface tension (Fig. 5a) [50]. This process is extremely rapid, typically occurring on a sub-millisecond timescale. In contrast, on the SL1000-SOCAL surface, the presence of liquid-like molecular brushes leads to the formation of a meniscus film around the droplets [32]. When the meniscus films of two neighboring droplets overlap, the smaller

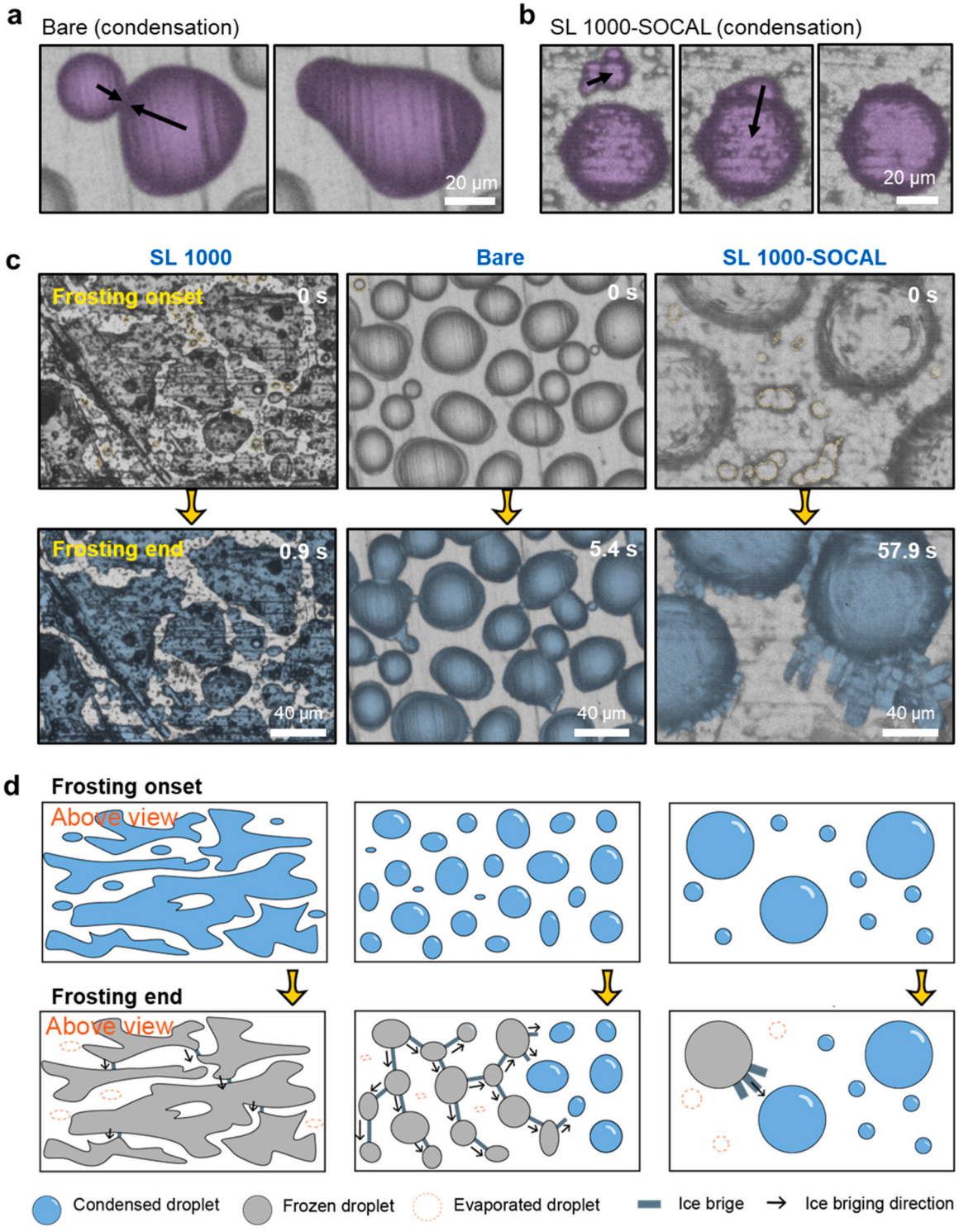

Fig. 5. Droplet coalescence and ice bridging dynamics during condensation and frosting. Representative time-lapse images showing droplet coalescence dynamics of (a) bare Al and (b) SL1000-SOCAL coated Al samples. (c) Time-lapse images and (d) schematics showing frost propagation dynamics. Schematics not to scale. Gravity points into the page.

droplet is more prone to forming an asymmetric meniscus relative to the larger one [51,52]. This asymmetry induces a capillary attraction that drives the smaller droplet to spontaneously migrate toward the larger droplet (Fig. 5b) [53,54], ultimately resulting in a broader droplet size distribution compared to the other two surfaces. Second, the higher hydrophobicity of the SL1000-SOCAL surface represents an increased nucleation barrier, suppressing condensation nucleation [55]. This results in a reduced droplet number density and, consequently, a significantly increased inter-droplet spacing (Fig. 5c) [56]. The spatial distribution established during condensation directly influences subsequent ice bridging dynamics.

As shown in Figs. 5c and 5d, at the onset of frosting (i.e., when droplet freezing first appears within the field of view), the relatively small inter-droplet spacing on bare and SL1000 surfaces enables rapid formation of ice bridges between frozen and neighboring unfrozen droplets [57,58], thereby promoting fast frost propagation. In contrast,

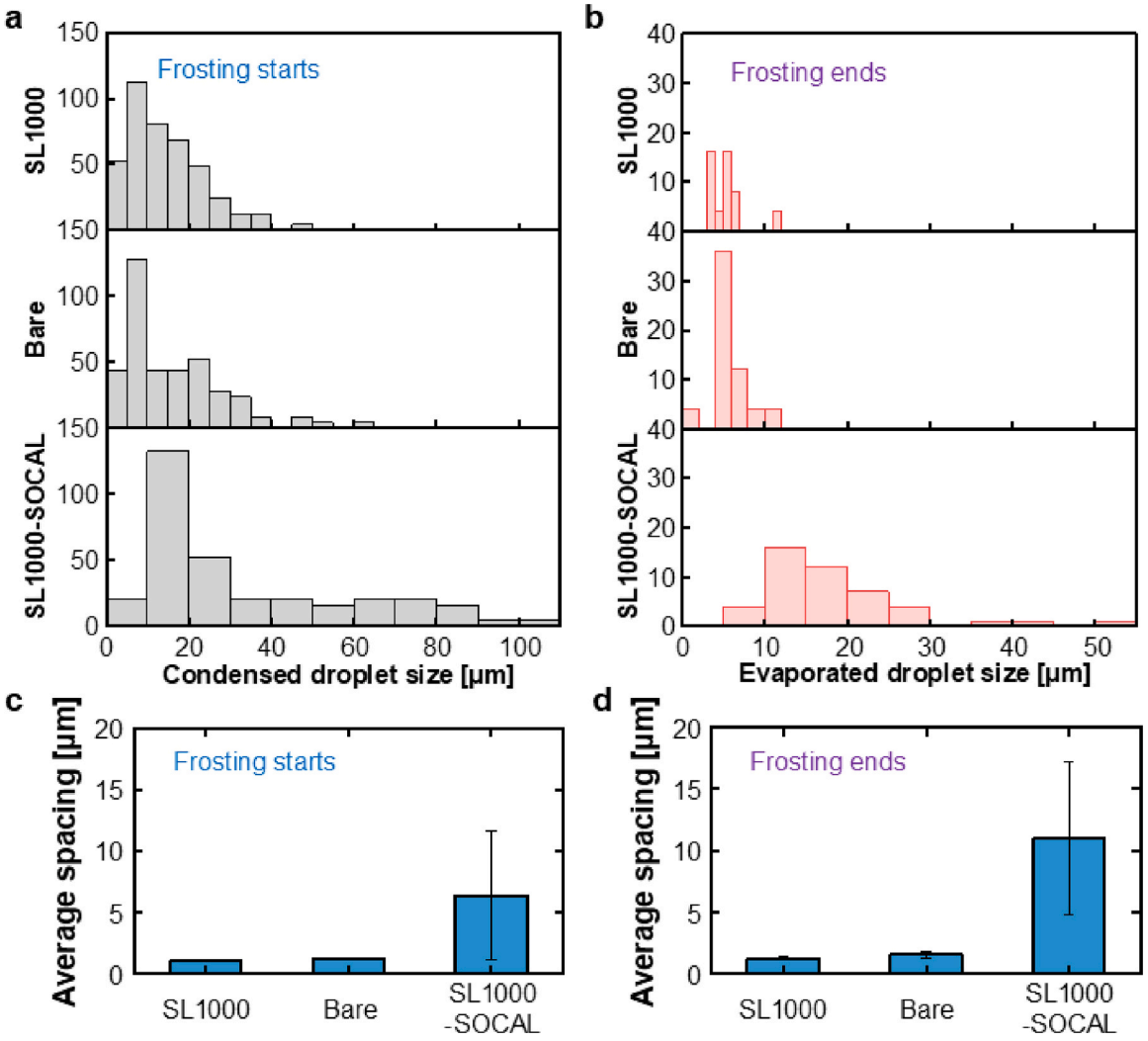

Fig. 6. Evolution of droplet size distribution and inter-droplet spacing before and after frosting. Statistical diameter distributions (a) at the onset of frosting for condensed droplets and (b) at the end of frosting for frozen droplets. (c) Average inter-droplet spacing at the onset of frosting for different surfaces. (d) Average spacing between frozen droplets at the completion of frosting. Error bars represent standard deviation, and all statistics are obtained from at least 30 independent measurements.

on the SL1000-SOCAL surface, the enlarged inter-droplet spacing significantly limits ice-bridge formation, leading to a reduced propagation rate of frost. It is worth noting that the latent heat released during droplet freezing can induce complete evaporation of some neighboring condensed droplets (circled in red in Fig. 5d) [59,60], which further alters the local droplet distribution and influences ice bridging dynamics.

To quantitatively capture the microscale differences in detail, we analyzed the evolution of droplet size distributions and their spatial arrangement (Fig. 6). At the onset of frosting, as shown in Fig. 6a, on SL1000 and bare surfaces, droplets are mainly confined to a narrow range of ~5–30 μm, with a dominance of smaller droplets. In contrast, the SL1000-SOCAL surface exhibits a significantly broader distribution, extending up to ~100 μm, indicating more pronounced droplet growth prior to freezing. This behavior can be attributed to two factors: (i) the liquid-like interface promotes the migration and coalescence of smaller droplets toward larger ones, enhancing size heterogeneity; and (ii) the higher hydrophobicity suppresses droplet freezing, thereby prolonging droplet growth time.

The statistical analysis of inter-droplet spacing (Fig. 6c) further reflects the spatial distribution characteristics. On the SL1000 and bare surfaces, the average inter-droplet spacing remains at ~1 μm, whereas on the SL1000-SOCAL surface it increases to ~6 μm, corresponding to a ~5–6-fold enhancement. This result indicates that the SL1000-SOCAL surface establishes a sparser droplet distribution during condensation. Despite the larger droplet spacing, the larger droplet size leads to an increased droplet surface area. Upon droplet freezing, due to the intrinsic vapor pressure difference between ice and liquid water, the frozen droplet acts as a vapor sink while the surrounding unfrozen droplets act as vapor sources [61], driving vapor transport and subsequent ice-bridge growth. Thus, SL1000-SOCAL surface with a larger droplet surface area may enhance vapor capture during ice bridge growth. In addition, the latent heat released during droplet freezing can induce complete evaporation of neighboring small droplets [60,61], further intensifying this droplet evaporation process.

Consistently, as shown in Fig. 6b, the size distribution of droplets undergoing evaporation during droplet freezing and ice bridging process also exhibits pronounced differences. On the SL1000 and bare surfaces, evaporating droplets are mainly distributed within ~3–12 μm. In contrast, on the SL1000-SOCAL surface, the distribution shifts toward larger sizes, primarily within ~10–25 μm and extending beyond 50 μm. This evaporation-driven mass redistribution further modifies the spatial arrangement of droplets. Therefore, at the completion of frosting (*i.e.*, when all droplets have frozen), a significant divergence in inter-droplet

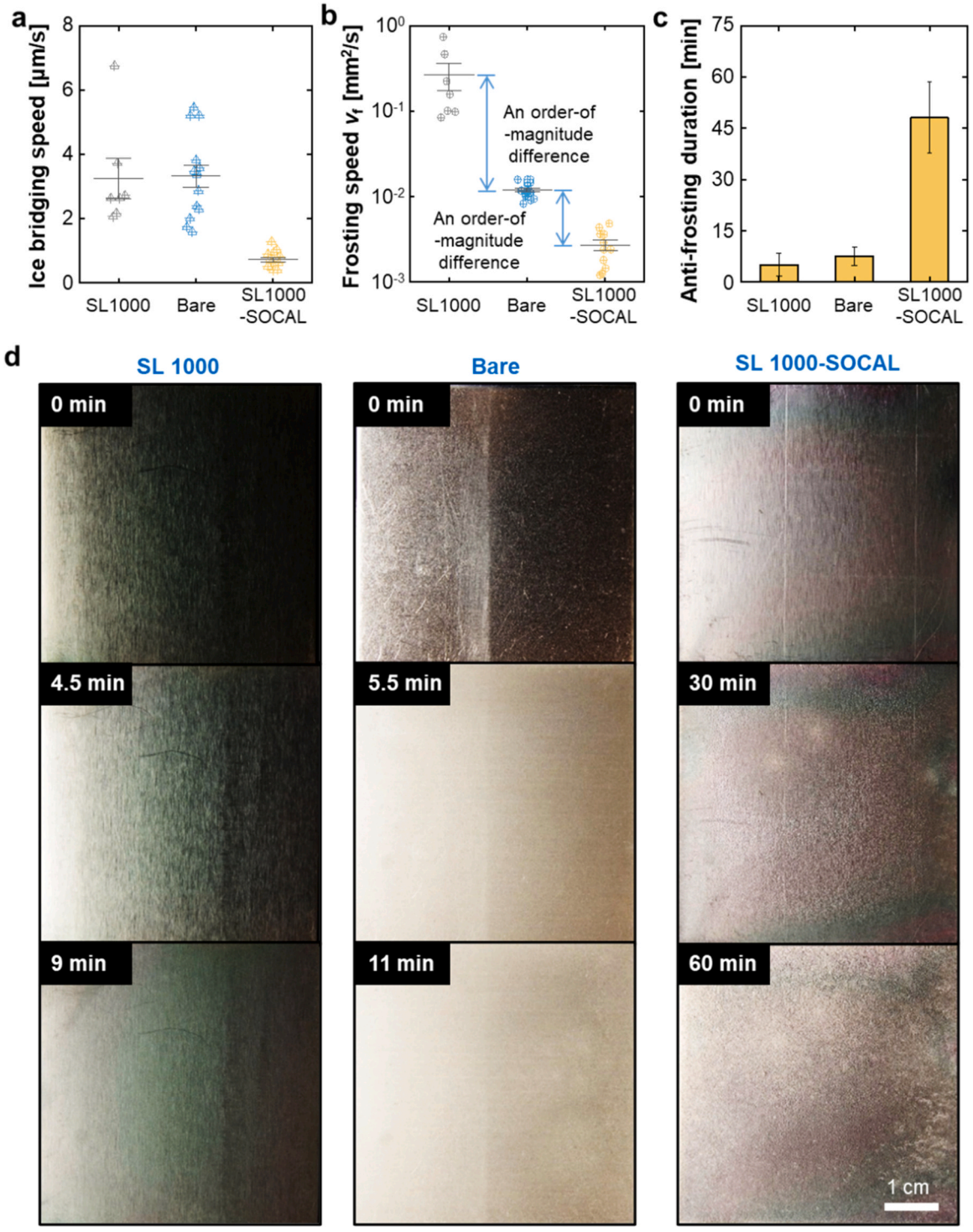

Fig. 7. Ice-bridging and frosting behavior. Comparison of (a) ice bridge propagation speed, (b) frost area propagation speed, and (c) frost-free duration. Symbols represent individual measurements, and horizontal lines indicate mean values with error bars showing standard deviation. (d) Time-resolved images of frost evolution. Time of 0 min is defined as the onset of frost occurrence. Gravity points into the page.

spacing is observed. The average spacing on SL1000 and bare surfaces remains at ~1–1.5 μm, whereas it increases to ~11 μm on the SL1000-SOCAL surface, corresponding to ~7–8 times that of bare and nearly one order of magnitude higher than that of SL1000. These results demonstrate that the SL1000-SOCAL surface not only establishes a sparse droplet distribution during condensation, but also continuously amplifies inter-droplet spacing throughout droplet freezing over the surface, thereby weakening ice bridging process between neighboring droplets and effectively suppressing frost spreading.

Fig. 7 compares the ice bridging speed, frost propagation rate, and the corresponding anti-frosting duration on SL1000, bare, and SL1000-SOCAL surfaces. As shown in Fig. 7a, the ice bridging speed is substantially suppressed on SL1000-SOCAL, remaining below ~1.5 μm s^{-1}, whereas bare exhibits intermediate values (~2–5 μm s^{-1}), and SL1000 shows the highest propagation speed on the order of ~3–7 μm s^{-1}. This trend becomes even more pronounced at the macroscopic scale. As

shown in Fig. 7b, the frosting area propagation rate on SL1000-SOCAL is on the order of 10^{-3} mm^2 s^{-1}, which is nearly two orders of magnitude lower than that on SL1000 ($\sim 10^{-1}$ mm^2 s^{-1}) and approximately one order of magnitude lower than that on bare ($\sim 10^{-2}$ mm^2 s^{-1}). The clear order-of-magnitude reduction indicates a strong suppression of frost spreading with increasing surface functionality. Consistently, the anti-frosting duration shown in Figs. 7c and 7d exhibits an opposite trend. The SL1000-SOCAL surface significantly prolongs the anti-frosting time to ~45–60 min, which is approximately 4–6 times longer than that on bare (~8–12 min) and nearly an order of magnitude longer than that on SL1000 (~4–6 min). Overall, these results demonstrate a strong correlation between microscale ice bridging dynamics and macroscale frosting behavior, where the suppressed ice bridging process on SL1000-SOCAL leads to a pronounced reduction in frosting propagation and a substantial extension of anti-frosting performance.

3.3. Corrosion resistance and coating integrity of SL1000-SOCAL-coated samples

In many applications, corrosion resistance and coating integrity are important metrics in addition to anti-frosting performance, because air-side HXs are continuously exposed to condensate [62,63]. Figs. 8a and

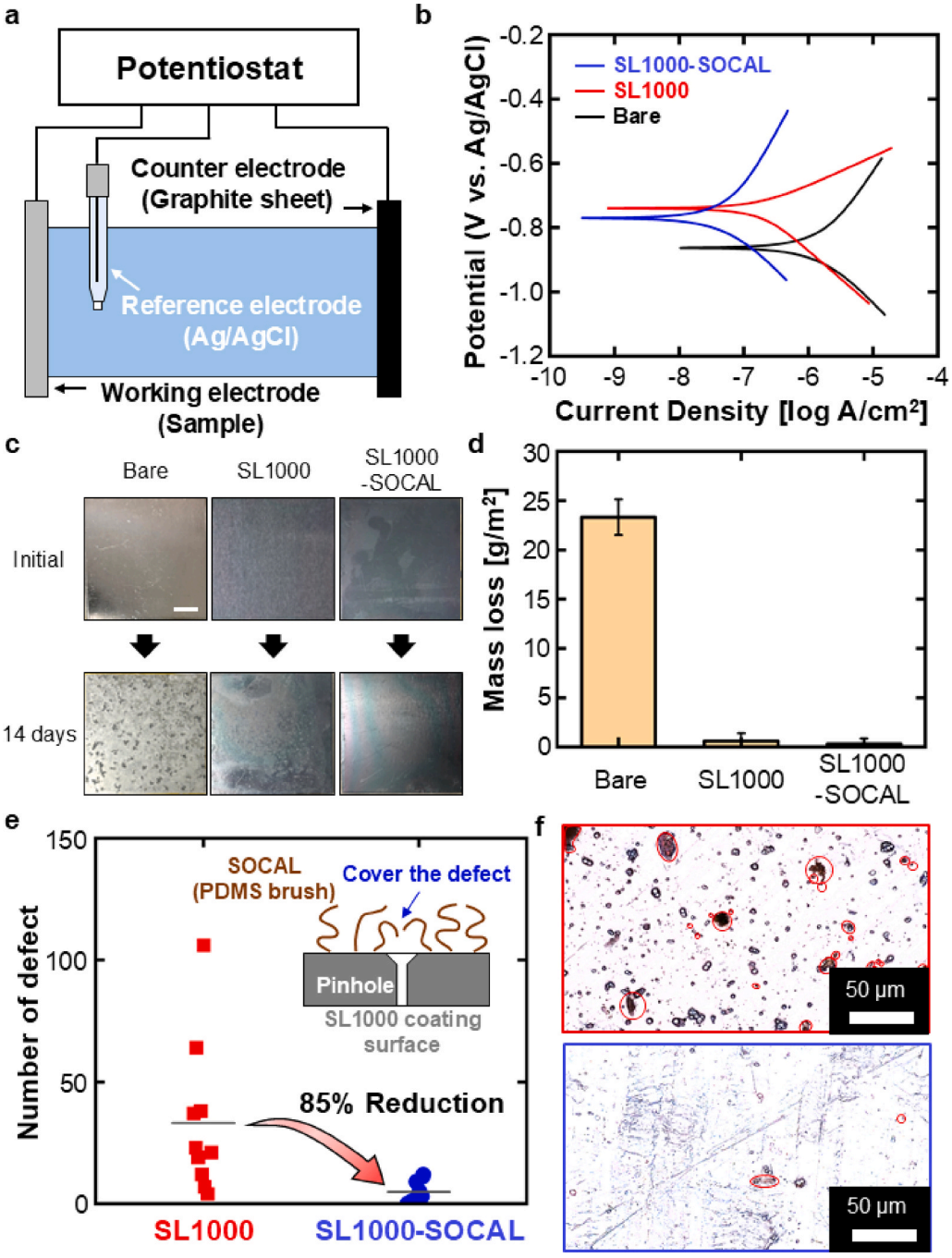

Fig. 8. Corrosion resistance and coating integrity. (a) Schematic diagram of the electrochemical experimental setup to quantify anti-corrosion performance. Schematic not to scale. (b) Representative Tafel plots of bare, SL1000, and SL1000-SOCAL samples. (c) Photographs of seawater acetic acid test before and after 14 days and (d) corresponding mass loss per unit area. (e) Quantification of surface defect by Cu electrodeposition and (f) representative optical images of SL1000 and SL1000-SOCAL samples. The defect number of (e) is quantified over a surface area of 211.73 × 282.40 μm^2.

8b show a schematic illustration of the electrochemical configuration used for the potentiodynamic polarization test and the corresponding Tafel plot, respectively. While the corrosion potentials of the three samples (bare, SL1000, and SL1000-SOCAL) were relatively similar (-852.0 ± 18.2 mV, −795.3 ± 49.7 mV, and −778.0 ± 46.5 mV, respectively), both the SL1000 (0.31 ± 0.16 μA/cm^2) and SL1000-SOCAL (0.16 ± 0.09 μA/cm^2) samples exhibited much lower corrosion current densities than the bare Al (1.57 ± 0.52 μA/cm^2) surface. In particular, the SL1000 sample also showed an 80.5% lower corrosion current density than bare Al, indicating that the SL1000 intermediate layer effectively acts as a protective barrier and prevents interaction with the corrosive electrolyte.

The accelerated corrosion test (SWAAT) results are consistent with the polarization measurements. After 14 days of SWAAT exposure, the bare Al surface underwent severe corrosion and extensive surface degradation, whereas the SL1000 and SL1000-SOCAL coatings remained in a comparatively initial state, as shown in Fig. 8c. According to the previous studies [64], 1 day of SWAAT exposure is equivalent to 9–12 months of corrosion in a coastal environment. From this point of view, 14 days of SWAAT is comparable to 10.5–14 years of corrosion in a coastal environment. More specifically, Fig. 8d shows the quantification of the mass loss after 14 days of SWAAT, both SL1000 (0.61 ± 0.77 g/m^2) and SL1000-SOCAL (0.30 ± 0.56 g/m^2) samples dramatically reduced the material loss compared with the bare one (23.32 ± 1.81 g/m^2).

The SL1000-SOCAL coating demonstrated superior results in both corrosion resistance experiments. As mentioned above, this is presumed to be due to the defect-free-like characteristics achieved by the freely movable SOCAL brushes covering surface defects [33]. To verify this, the surface defects of SL1000 and SL1000-SOCAL were quantified using the Cu electrodeposition method. Copper is preferentially deposited at through-thickness pinholes or discontinuities where the conductive Al substrate is locally exposed. The statistical results show that the SL1000-SOCAL samples (80 ± 73 counts/mm^2) reduced the number of detectable defects by ~ 85.5% relative to the SL1000 sample (554 ± 521 counts/mm^2), as shown in Fig. 8e. The representative optical microscope images in Fig. 8f are consistent with these results: numerous Cu-marked defect sites are observed on SL1000 surface, whereas only a few isolated defects remain after SOCAL treatment. These results show that the superior corrosion resistance of the SL1000-SOCAL surface arises from three complementary effects. First, the SL1000 intermediate layer provides an improved barrier against electrolyte ingress and electrochemical reactions. Second, the corrosion droplets can be easily removed from the surface by hydrophobic nature and low CAH of the SOCAL coating. Lastly, the SOCAL layer exhibits defect-free characteristics by covering the pinhole defects that can serve as initiation sites for localized corrosion. The exceptional corrosion stability and coating integrity of SOCAL coatings may provide a key to achieving long-term stable operating performance for HX applications.

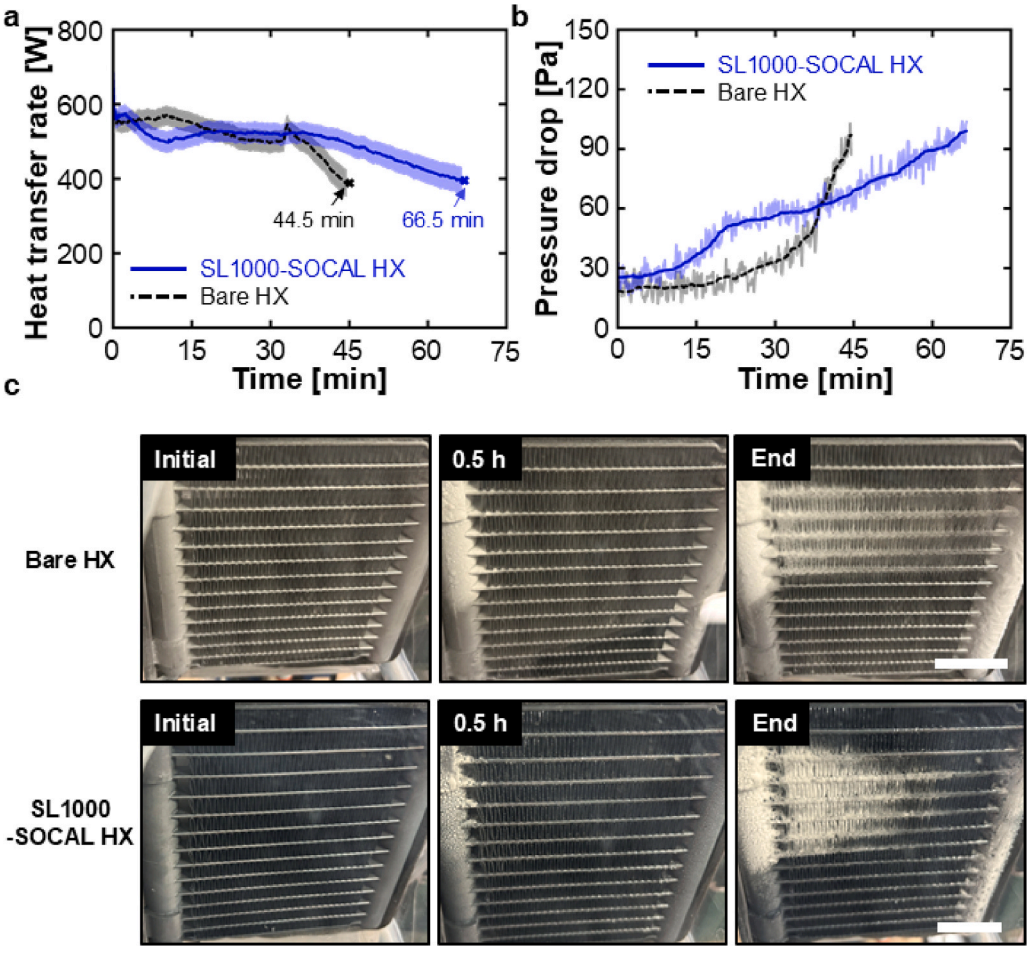

Fig. 9. Heat exchanger frosting performance of the bare and SL1000-SOCAL HX under the baseline condition. Representative graphs of (a) heat transfer rate and (b) pressure drop according to time. The arrows in (a) indicate the time at which the heat transfer rate decreased to 70% of its initial value. The shaded regions in (a) and (b) represent the propagated experimental uncertainties of the heat transfer rate and the experimental errors of the pressure drop. (c) Photographs of frost accumulation on the frontal area of the bare and SL1000-SOCAL HXs at the initial state, after 0.5 h, and at the end of the frost test. Scale bars are 3 cm. HXs are vertically oriented in the photographs (gravity points down).

3.4. Heat exchanger anti-frosting performance of SL1000-SOCAL coating samples

Fig. 9 compares the frosting behavior of the bare and SL1000-SOCAL-coated louver-fin microchannel HXs under the C2 (baseline conditions, air velocity of 2 m/s and HX liquid inlet temperature of −5°C). As shown in Fig. 9a, both HXs initially exhibited comparable heat transfer rates, but the degradation behavior diverged as frosting progressed. The bare HX showed a relatively rapid decrease in heat transfer rate after the initial frosting stage and reached 70% of it at 48.3 ± 8.8 min, whereas the SL1000-SOCAL HX maintained a higher heat transfer rate for a substantially longer period and reached the same criterion at 71.8 ± 14.3 min. This corresponds to a ~48.6% extension in the useful frosting time, defined as the time when frosting is occurring on the HX and heat transfer is not degraded beyond 30% when compared to the nominal frost-free value.

The air-side pressure drop evolution in Fig. 9b shows a consistent trend. Although both samples started from a similar initial pressure drop, the bare HX exhibited an earlier onset of rapid pressure drop increase, indicating faster air-pass-blockage by frost formation. In contrast, the SL1000-SOCAL HX showed a more gradual increase in pressure drop, implying delayed frost accumulation within the louver passages. Furthermore, the pressure drop at the end stage (when 70% of the initial heat transfer rate was reached) was similar in both cases. This implies that, at the end stage, a comparable degree of air-pass-blockage occurred and consequently, a similar amount of frost was formed in both scenarios. The photographs in Fig. 9c further supports this interpretation. After 0.5 h, the bare HX already exhibited more severe frost accumulation over the frontal area, whereas the SL1000-SOCAL HX retained more open-air passages. Following the coolant flow path, it can be observed that frosting begins from the top-left corner in both the bare and SL1000-SOCAL HXs. By the end of the test, the SL1000-SOCAL HX showed a comparable density of the blocked frost layer with that of the bare one. It should be noted that, in the case of the SL1000-SOCAL HX, frost formation tends to exhibit a more distinct droplet-like morphology as shown in Fig. 9c. This phenomenon occurs because moisture in the air condenses on the surface, forming dropwise condensation, which subsequently undergoes a phase transition to form ice. Conversely, with the bare HX, no characteristic droplet-shaped ice was observed on the surface, as the condensed liquid formed a thin water film over the surface before undergoing a phase transition.

Fig. 10 shows the heat transfer performance of the bare and SL1000-SOCAL HXs under additional test conditions. It should be noted that the coupon-level ice-bridging experiments were conducted under quiescent conditions, whereas the HX experiments involve forced convection. When the inlet air velocity was 1 m/s (C1), the useful frosting time increased from 43.5 ± 7.8 min for the bare HX to 61.3 ± 12.8 min for the SL1000-SOCAL HX (Fig. 10a). When the inlet air velocity was increased to 3 m/s (C3), the useful frosting time increased from 94.2 ± 26.2 min to 151.3 ± 22.5 min (Fig. 10b). In the lower-HX inlet-temperature case (C4, HX inlet temperature of −7°C), the SL1000-SOCAL HX still outperformed the bare HX, extending the useful frosting time from 47.2 ± 10.8 min to 59.3 ± 8.0 min as shown in Fig. 10c. Despite that airflow introduces additional effects, including aerodynamic shear on condensed droplets and enhanced convective heat and mass transfer, the SL1000-SOCAL HX consistently extended the useful frosting time relative to the bare HX across the investigated air velocities of 1–3 m/s, corresponding to improvements of approximately 41.0%, 48.6%, and 60.7%, respectively. Therefore, the coupon-scale results are interpreted as the intrinsic mechanistic basis for the observed anti-frosting behavior, while the HX-level results demonstrate that the resulting performance advantage persists when airflow-induced transport and shear effects are

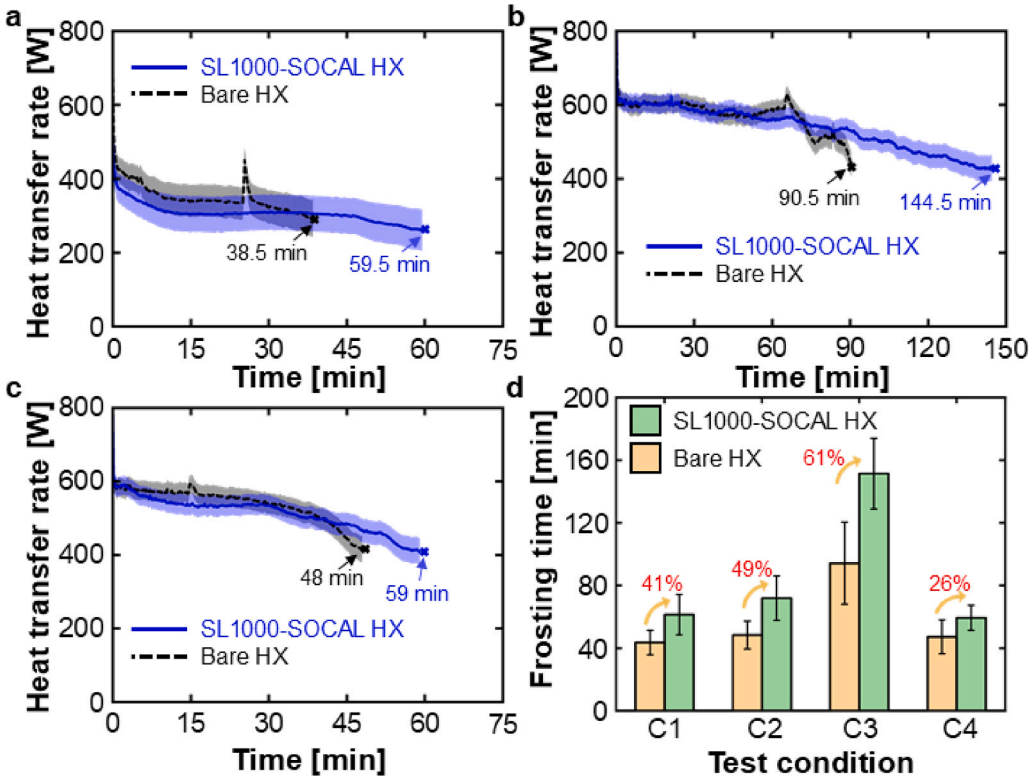

Fig. 10. Effect of operating conditions on the HX-level frosting performance of the bare and SL1000-SOCAL HXs. Representative heat transfer rate graphs according to the time under (a) C1, (b) C3, and (c) C4. The arrows in (a)–(c) indicate the time at which the heat transfer rate decreased to 70% of its initial value. The shaded regions in (a)–(c) represent the propagated experimental uncertainties of the heat transfer rate. (d) Summary of total frosting time for C1–C4, where frosting time is defined as the elapsed time required for the heat transfer rate to decrease to 70% of its initial value. Error bars represent standard deviation from 3 independent measurements.

present.

Overall, the summary in Fig. 10d provides 3 implications for improving the heat transfer performance of the SL1000-SOCAL HX. (1) In all experiments, SL1000-SOCAL HX improved the frosting time by at least 25.8% compared to bare HX, although the magnitude of improvement depended on the operating condition. (2) As the air velocity increases, the shear force generated by the airflow increases, resulting in a relatively larger gap of frosting time between two HX samples. Similarly, as the air velocity decreases, the gap gets smaller. (3) As the coolant temperature at the HX inlet decreases, the frosting-delaying effect provided by SL1000-SOCAL coatings diminishes. This implies that once frosting has already occurred, the SOCAL coating offers no further efficacy in either removing the frost or delaying its further accumulation. Consistent with the frosting mechanisms identified in the coupon-level experiments, these observations provide a mechanistic basis for understanding the improved HX performance. At higher air velocities, the benefit associated with increased inter-droplet spacing and consequently suppressed ice-bridge propagation may become more pronounced, as occasional larger or weakly retained condensate droplets can potentially be displaced or removed by aerodynamic shear before participating in ice-bridge formation. In contrast, at lower coolant temperature, the stronger subcooling accelerates freezing and frost deposition, which reduces the benefit of the coating.

Figs. 11 and 12 further compare the 3 h cyclic frosting/defrosting behavior of the bare and SL1000-SOCAL HX. During the 3 h cyclic frosting/defrosting test, the overall pattern of both HX samples is similar. During each frosting cycle, the heat transfer rate decreases, and the corresponding pressure drop increases; however, during the defrosting cycle, the pressure drop decreases rapidly, and the initial heat transfer rate increases again when the re-frosting cycle starts. Fig. 11a presents the variations in the heat transfer rate for the bare HX during the cyclic frosting/defrosting test, where each frosting phase was terminated when the heat transfer rate dropped to 70% of its initial value. On reaching this threshold, the pump on the closed-loop coolant side was shut off for 6 min for defrosting. In the case of the bare HX, a distinct difference in frosting duration is observed between the first frosting cycle and the subsequent cycles (4th–6th). This is attributed to residual melted water remaining on the louver fins after defrosting, which accelerated frost formation during the subsequent re-frosting phase [65,66]. This phenomenon is even clearer when examining the pressure drop trends shown in Fig. 11b. Compared to the initial baseline (indicated by the red dotted line), the initial pressure drop values during the re-frosting cycles appear slightly elevated. This is believed to be caused by the formation of droplet bridges across the louver fins, which partially obstructed airflow [66,67].

Fig. 12a shows the heat transfer rate profile during the cyclic frosting/defrosting test of SL1000-SOCAL HX. Unlike the bare HX, the SL1000-SOCAL HX appears to undergo a more complete surface refresh during defrosting, owing to the low contact-line pinning due to the slippery characteristics of the SOCAL interface. The meltwater during the defrosting experiences much lower friction resistance and can be more readily separated from the louver fins by the air-side shear, allowing each subsequent re-frosting cycle to restart from a state close to the pristine conditions, as evidenced by the repeated recovery of the initial heat transfer rate and pressure drop toward the green and red dotted lines in Figs. 12a and 12b. As a result, it was confirmed that SL1000-SOCAL HX can have higher energy efficiency characteristics, with a defrosting cycle of 50% of that of the bare HX (3.3 ± 0.6 cycles vs.6.7 ± 0.6 cycles) during a 3 h cyclic frosting/defrosting test .

Repeated frosting and defrosting can impose both thermal and mechanical stress on coating layers. Differential thermal expansion between a coating and its substrate can generate cyclic interfacial stresses and initiate cracking, and repeated ice formation, melting, and water removal can promote surface damage and deterioration of wetting characteristics [68]. In addition, in our previous study on repetitive frosting and defrosting [69], various anti-frosting surfaces, including SLIPS, during atmospheric frosting/defrosting cycles can undergo chemical degradation, leading to the formation of local high-surface-energy defects, increased condensate retention, or lubricant drainage. To evaluate possible degradation caused by these

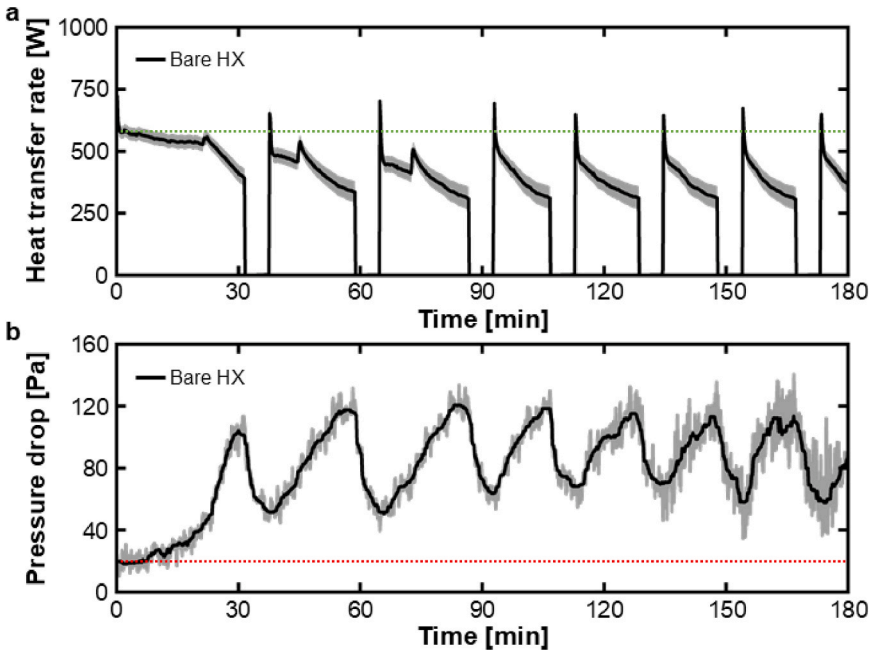

Fig. 11. Cyclic frosting/defrosting behavior of the bare HX under C2 over a 3 h test period. Representative graph of (a) heat transfer rate and (b) air-side pressure drop according to time. Defrost was initiated when the heat transfer rate decreased to 70% of its initial value by stopping coolant circulation for 6 min. The shaded regions in (a) and (b) represent the propagated experimental uncertainties of the heat transfer rate and the experimental errors of the pressure drop. The green dotted line in (a) denotes the initial heat transfer rate of the first frosting cycle, and the red dotted line in (b) denotes the initial pressure drop of the pristine HX before frosting. The incomplete recovery toward these reference dotted lines after defrost indicates residual melted water retention and a penalized re-frosting state in subsequent cycles.

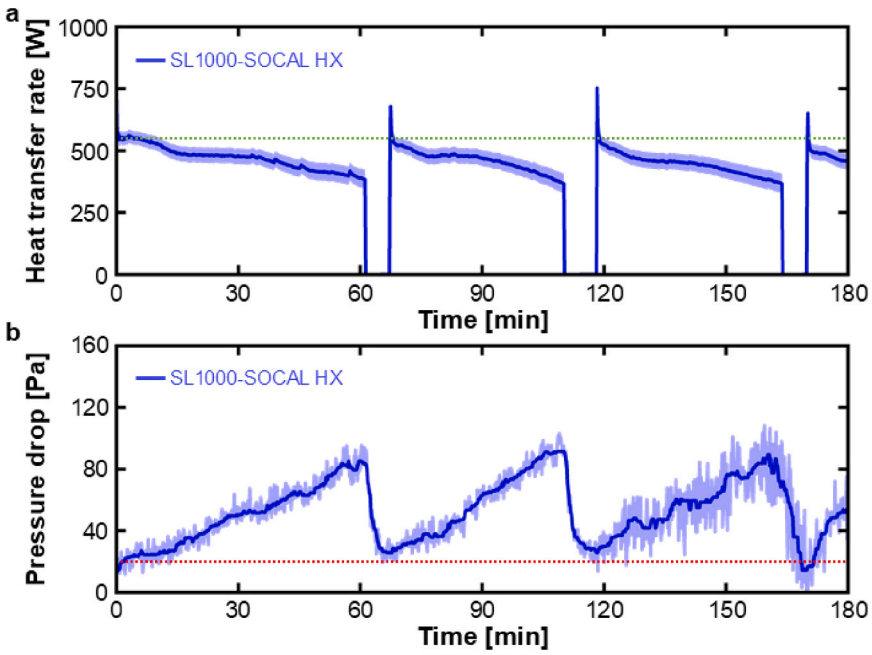

Fig. 12. Cyclic frosting/defrosting behavior of the SL1000-SOCAL HX at C2 conditions over a 3 h test period. Representative graph of (a) heat transfer rate and (b) air-side pressure drop according to time. Defrost was initiated when the heat transfer rate decreased to 70% of its initial value by stopping coolant circulation for 6 min. The shaded regions in (a) and (b) represent the propagated experimental uncertainties of the heat transfer rate and the experimental errors of the pressure drop. The green dotted line in (a) denotes the initial heat transfer rate of the first frosting cycle, and the red dotted line in (b) denotes the initial pressure drop of the pristine HX before frosting. The repeated recovery toward these reference lines indicates more effective removal of defrosting melted water and a refreshed surface prior to each re-frosting cycle.

repeated frosting/defrosting cycles, we conducted an additional 50-cycle frosting/defrosting durability test using the SL1000-SOCAL HX. The test was conducted under a C5 condition, with an HX inlet temperature of −7°C and an inlet air velocity of 0.5 m/s. After completing the 50-cycle exposure, the same SL1000-SOCAL HX was retested under C2 conditions to determine whether its anti-frosting performance had degraded. As shown in Fig. 13a, the heat transfer rate profiles before and after the 50-cycle test remained comparable. Specifically, compared to the anti-frosting performance (71.8 ± 14.3 min) of the existing C2 condition, no performance degradation was observed in the re-test (75.0 ± 9.3 min) after 50 cycles. Fig. 13b shows SEM images of the SL1000-SOCAL HX surface before and after performing the 50-cycle repeated frosting/defrosting test. No observable morphological degradation, such as cracking or delamination, was detected after 50 cycles.

Despite these efforts to demonstrate coating durability through repeated frosting and defrosting cycles, 50 cycles remain insufficient to establish long-term, seasonal, or lifetime durability. For example, Ma et al. [70] evaluated the durability of a frostphobic surface over 1000 frosting/defrosting cycles. Although their surface architecture and experimental configuration differ from those employed in our study, their work demonstrates that substantially longer cycling tests are required before long-term durability can be conclusively claimed. Nevertheless, our results provide direct HX-level evidence that the SL1000-SOCAL coating retained its anti-frosting functionality and exhibited no observable surface damage during the tested 50 cycles.

3.5. Annual economic impact analysis of SL1000-SOCAL-coated HXs

The analysis evaluated three independent prolonged experimental runs for both the bare and SOCAL-coated HXs under C2 conditions.

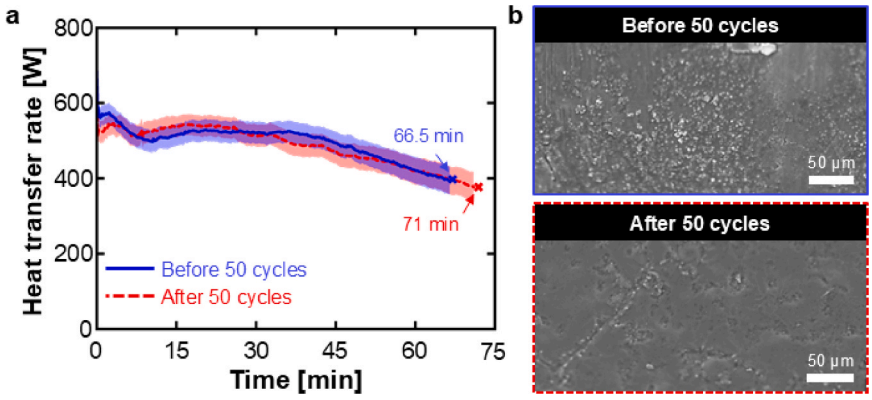

Fig. 13. Retention of the anti-frosting performance of the SL1000-SOCAL HX after 50 frosting/defrosting cycles. (a) Representative graphs of heat transfer rate according to the time under the C2 condition before and after the 50-cycle exposure. The arrows indicate the time at which the heat transfer rate decreased to 70% of its initial value. The shaded region represents the propagated experimental uncertainties of the heat transfer rate. (b) Representative SEM images of the SL1000-SOCAL HX surface before and after 50 frosting/defrosting cycles.

Because the system operates dynamically, cycling between active heating and inactive defrosting, the values reported are time-averaged over the entire duration of the stable cycles. The aggregated results clarify the compounding thermal penalty of operating an uncoated coil under frosting conditions. Because the uncoated HX suffers from rapid frost blockage, its active heating phases are shortened, forcing the system into frequent defrost cycles. During these defrost periods, the compressor shuts off ($Q_{heat} = 0$ W), forcing the auxiliary PTC heater to run at its maximum capacity of 1500 W to maintain the room temperature. Because the bare coil spends a large percentage of its total operating time in this defrost "downtime," its time-averaged performance is severely affected. Across its stable cycles, the bare HX maintained an average evaporator load of just 249.5 W and an average compressor power of 380.9 W. Consequently, the heat pump cycle time-averaged heating output was only 630.4 W. To continuously meet the 1500 W room demand across all operational phases, the system was forced to rely heavily on the auxiliary electric heater, requiring a time-averaged backup of 869.6 W.

In contrast, the SL1000-SOCAL HXs significantly outperformed the baseline by minimizing defrost frequency and sustaining a much higher time-averaged evaporator load of 408.7 W. While it may seem counterintuitive that the SOCAL coating draws a higher average compressor power (517.0 W vs. 380.9 W), this is in fact a key indicator of superior performance. The vapor-compression cycle is efficient (COP > 1), whereas the PTC heater operates at a 1:1 efficiency. By resisting water retention, the SOCAL coil keeps the compressor running longer and pumping more thermodynamic heat ($Q_{heat} = 925.7$ W), reducing the reliance on the inefficient PTC heater to just 574.3 W. By shifting the heating load away from the PTC heater and back onto the compressor, the SOCAL coating improved the effective system COP from 1.20 to 1.37. The application of SOCAL coating yields a substantial reduction in system energy consumption. By mitigating water retention on the coils after defrosting cycles, the performance degradation of SL1000-SOCAL HX is minimal over subsequent cycles, thereby minimizing the activation of high-draw auxiliary electric heaters. Extrapolated over the 1701 annual heating hours standard for AHRI Region IV, the SOCAL coating reduces annual energy consumption by 270.9 kWh compared to the uncoated baseline. While the absolute cost savings of ~$40 per year may initially appear modest, it is critical to note that this experimental model represents a fractional-scale 1.5 kW heating demand. When these efficiency gains (a 12.7% reduction in annual energy consumption and 14.2% improvement in effective system COP) are scaled up to standard 3-ton to 5-ton (10 kW to 15 kW) residential heat pumps or integrated into large-scale commercial and EV thermal management systems, the operational energy and cost savings become more significant. Annual economic projections are summarized in Table 4.

Although the present study clearly demonstrates the anti-frosting benefit of the SL1000-SOCAL coating at both the coupon- and HX-levels, several limitations should be noted. First, the HX experiments were performed on a single louver-fin microchannel geometry within a limited operating window (open-loop), and therefore, the quantitative improvement in frosting time may vary with test conditions, such as fin geometry, configuration, air temperature, and air humidity. Second, to accurately quantify actual energy efficiency degradation and calculate the associated costs, it is essential to verify system-level performance by considering the loads and operational dynamics of all other components. Lastly, comprehensive durability verification of coated HXs is required, involving repeated frosting/defrosting cycles over extended periods in a reversible air source heat pump system. Therefore, future research should focus on assessing energy performance within more practical operating environments by expanding the scope of operating conditions and HX geometries. Furthermore, it needs to be verified through long-term testing, comprehensive operating conditions, and system-level performance evaluations.

Table 4
System-level performance and annual economic projections.

Parameter	Bare HX	SL1000-SOCAL HX
Average evaporator load (Q_{refr})	249.5 W	408.7 W
Average compressor power (W_{cp})	380.9 W	517.0 W
Average heat pump output (Q_{heat})	630.4 W	925.7 W
Average PTC backup power	869.6 W	574.3 W
Average total electrical power	1250.5 W	1091.4 W
Effective system COP	1.20	1.37
Total annual energy input	2,127.2 kWh	1,856.3 kWh
Total annual heating cost	$319.08	$278.45

4. Conclusions

In this study, an SL1000-SOCAL coating was applied to an aluminum louver-fin microchannel HX, and its anti-frosting performance was evaluated from coupon-level interfacial behavior to HX-level frosting/defrosting operation. The major findings are summarized as follows:

First, the SL1000-SOCAL surface exhibited hydrophobic and slippery characteristics with a CA of 103.7° and a CAH of 2.3°. The liquid-like SOCAL interface promoted droplet migration and coalescence, broadened the condensate-size distribution, and increased the inter-droplet spacing. Consequently, ice-bridge propagation and macroscopic frosting speed were substantially suppressed. The resulting anti-frosting duration was approximately 45–60 min, which was 4–6 times longer than that of bare Al and nearly one order of magnitude longer than that of SL1000.

Second, the SL1000-SOCAL coating exhibited the lowest corrosion current density of 0.16 ± 0.09 μA/cm^2 and minimal mass loss of 0.30 ± 0.56 g/m^2 after 14 days of SWAAT. Cu-electrodeposition-based defect quantification further showed that SOCAL treatment reduced the number of detectable coating defects by 85.5% relative to the SL1000 coating. These excellent anti-corrosion characteristics can be attributed to the defect-free nature of the SOCAL polymer brush. After the accelerated 50-cycle frosting/defrosting durability test, the useful frosting time under the baseline C2 condition remained comparable. Also, no observable cracking or delamination was detected in the post-cycling SEM images.

Lastly, the SL1000-SOCAL HX delayed heat transfer rate degradation and air-side pressure drop growth under all investigated operating conditions (C1–C4), extending the useful frosting time by 25.8–60.7% relative to the bare HX. During the separate 3 h cyclic frosting/defrosting test, the mean number of required defrost events decreased from 6.7 ± 0.6 for the bare HX to 3.3 ± 0.6 for the SL1000-SOCAL HX. The repeated recovery of the initial heat transfer rate and pressure drop following defrosting was consistent with more effective meltwater removal and surface refresh enabled by the low contact-line pinning of the SOCAL interface. Under the simplified annual heating scenario considered in this study, this improvement was projected to increase the effective system COP from 1.20 to 1.37 and reduce annual energy consumption by 270.9 kWh (12.7%), corresponding to an illustrative annual heating-cost reduction of ~$40 for a representative 1.5 kW heating load.

Overall, the combined coupon- and HX-level results demonstrate that lubricant-free SOCAL coatings offer a promising approach for simultaneously improving the frosting, defrosting, corrosion, and cyclic durability characteristics of compact airside HXs.

CRediT authorship contribution statement

Jung Bin Yang: Writing – review & editing, Writing – original draft, Visualization, Validation, Methodology, Investigation, Data curation, Conceptualization. **Siyan Yang:** Writing – review & editing, Writing – original draft, Visualization, Validation, Methodology, Investigation, Data curation, Conceptualization. **Donghyeon Yoo:** Writing – original draft, Validation, Methodology, Investigation, Data curation. **Kaushik Chettiar:** Writing – original draft, Validation, Methodology,

Investigation, Data curation. **Zihao Liu:** Visualization, Validation, Methodology, Investigation, Data curation. **Sujan Dewanjee:** Visualization, Validation, Investigation, Data curation. **Garrett Fleetwood:** Visualization, Validation, Investigation, Data curation. **Omar Abdelhamid:** Validation, Methodology, Investigation, Data curation. **Md Rakibul Hasan Roni:** Validation, Methodology, Investigation, Data curation. **Seungyeon Lee:** Validation, Methodology, Investigation, Data curation. **Cheng Zhang:** Validation, Methodology, Investigation, Data curation. **Ali Riahi:** Validation, Methodology, Investigation, Data curation. **Hyeonho Lee:** Validation, Methodology, Investigation, Data curation. **Dong Rip Kim:** Supervision, Methodology, Investigation. **Nenad Miljkovic:** Writing – review & editing, Visualization, Validation, Supervision, Project administration, Methodology, Investigation, Funding acquisition, Conceptualization.

Declaration of Competing Interest

The authors declare that they have no known competing financial interests or personal relationships that could have appeared to influence the work reported in this paper.

Acknowledgements

The team is thankful for the financial support provided by the Air Conditioning and Refrigeration Center (ACRC). The authors also acknowledge the use of SEM, FIB, XPS, and goniometer facilities at the Materials Research Laboratory Central Facilities at the University of Illinois, which were instrumental in this study. N.M. gratefully acknowledges funding support from the International Institute for Carbon Neutral Energy Research (WPI-I2CNER), sponsored by the Japanese Ministry of Education, Culture, Sports, Science and Technology.

References

[1] M. Hamid, M. Song, C. Yu-Hang Chao, M.A. Qaisrani, H. Shi, K. Shao, Z. Zhen, R. Gao, X. Zhang, L. Zhang, S.H. Hosseini, N. Ahmed, D.A. Uglanov, L. Pekař, Y. Chen, J. Liu, Can nature-inspired surface and interface designs offer practical solutions for anti-icing? Renew. Sustain. Energy Rev. 228 (2026) 116563.
[2] R. Gao, M. Song, C.Y.H. Chao, S. Lin, L. Zhang, X. Zhang, Review on condensation frosting and defrosting experiments for superhydrophobic surfaces, Appl. Therm. Eng. 236 (2024) 121691.
[3] J. Kim, S. Byun, J. Lee, K.-S. Lee, Frost growth behavior according to the cold surface inclination angle, Int. J. Heat Mass Transf. 146 (2020) 118841.
[4] D. Gibb, J. Rosenow, R. Lowes, N.J. Hewitt, Coming in from the cold: Heat pump efficiency at low temperatures, Joule 7 (9) (2023) 1939–1942.
[5] M.E. Konrad, B.D. MacDonald, Cold climate air source heat pumps: industry progress and thermodynamic analysis of market-available residential units, Renew. Sustain. Energy Rev. 188 (2023) 113739.
[6] J. Rosenow, D. Gibb, T. Nowak, R. Lowes, Heating up the global heat pump market, Nat. Energy 7 (10) (2022) 901–904.
[7] M. Olyaei, M.M. Alam, P. Patel, S. Yousaf, C.R. Bradshaw, N. Miljkovic, Performance evaluation of an electric vehicle vapor injection heat pump system during cold and hot start-up using dynamic system modeling, Int. J. Heat Mass Transf. 254 (2026) 127628.
[8] A. Wang, X. Yin, F. Jia, F. Cao, Y. Liu, X. Wang, Driving range evaluation based on different cabin thermal management goals of CO2 heat pumps for electric vehicles, J. Clean. Prod. 382 (2023) 135201.
[9] T. Yuksel, J.J. Michalek, Effects of regional temperature on electric vehicle efficiency, range, and emissions in the United States, Environ. Sci. Technol. 49 (6) (2015) 3974–3980.
[10] K. Shao, M. Song, Lifetime of air bubbles detached from the freezing front during icing, Appl. Phys. Lett. 127 (22) (2025) 222701.
[11] S. Byun, J. Won, J. Song, H. Jeong, K.-S. Lee, Modeling of frost formation under cryogenic conditions based on the hybrid physics-informed data-driven method, Int. Commun. Heat Mass Transf. 162 (2025) 108588.
[12] H.-Y. Ye, K.-S. Lee, Performance prediction of a fin-and-tube heat exchanger considering air-flow reduction due to the frost accumulation, Int. J. Heat Mass Transf. 67 (2013) 225–233.
[13] J.-S. Park, D.R. Kim, K.-S. Lee, Frosting behaviors and thermal performance of louvered fins with unequal louver pitch, Int. J. Heat Mass Transf. 95 (2016) 499–505.
[14] E. Bisengimana, J. Zhou, M. Binama, K. Zhao, S. Abbas, Y. Yuan, The frosting and soil imbalance performance issues of building heat pumps: an overview, Energy Build. 273 (2022) 112387.
[15] Y. Shen, H. Zou, S. Wang, Detection of frost growth and distribution on louver and offset strip fins of a microchannel heat exchanger using capacitance sensing approach, Int. J. Heat Mass Transf. 217 (2023) 124650.
[16] J. Liu, Y. Sun, W. Wang, J. Zhu, Performance evaluation of air source heat pump under unnecessary defrosting phenomena for nine typical cities in China, Int. J. Refrig. 74 (2017) 385–398.
[17] W. Wang, Y.C. Feng, J.H. Zhu, L.T. Li, Q.C. Guo, W.P. Lu, Performances of air source heat pump system for a kind of mal-defrost phenomenon appearing in moderate climate conditions, Appl. Energy 112 (2013) 1138–1145.
[18] Y. Liang, M. Song, L. Zhang, T. Xu, Q. Liu, W. Kuang, Experimental study on the distribution characteristics of condensation frosting and defrosting on a single vertical straight fin under constrained airflow conditions, Int. Commun. Heat Mass Transf. 172 (2026) 110695.
[19] W. Wei, Y. Guo, W. Wang, Z. Jiang, X. Zhang, C. Dai, Y. Sun, B. Li, S. Wang, C. Zhang, Development of a universal frosting rate prediction model for optimizing the defrosting control strategy of air source heat pumps, Energy 344 (2026) 139859.
[20] W. Wei, Z. Feng, Y. Sun, W. Wang, X. Jin, J. Zhang, C. Dai, Experimental investigation on the space heating performance of air source heat pump with vapor injection under frosting condition, J. Build. Eng. 90 (2024) 109327.
[21] C. Ma, X. Ge, H. Zheng, M. Song, W. Sheng, X. Chen, D. Fu, C. Dang, From common low temperature to ultra-low temperature: overview of frosting characteristics and defrosting techniques in equipment, Appl. Therm. Eng. 278 (2025) 127205.
[22] M. Song, S. Deng, C. Dang, N. Mao, Z. Wang, Review on improvement for air source heat pump units during frosting and defrosting, Appl. Energy 211 (2018) 1150–1170.
[23] S. Yang, B. Ji, Y. Feng, Y. Jin, W. Xu, J. Lu, X. Qin, H. Zhang, M. Li, Z. Xu, X. Liu, L. Xu, D. Wang, R. Wen, Z. Wang, S. Wang, X. Ma, Z. Wang, How surface charges affect interdroplet freezing, Proc. Natl. Acad. Sci. USA 122 (25) (2025) e2507849122.
[24] K.S. Boyina, A.J. Mahvi, S. Chavan, D. Park, K. Kumar, M. Lira, Y. Yu, A.A. Gunay, X. Wang, N. Miljkovic, Condensation frosting on meter-scale superhydrophobic and superhydrophilic heat exchangers, Int. J. Heat Mass Transf. 145 (2019) 118694.
[25] K.-S. Yang, J.-W. Zheng, K.-L. Wu, Y.-L. Wu, Performance of the frosting characteristics of fin-and-tube heat exchanger subject to superhydrophobic coating, Appl. Therm. Eng. 235 (2023) 121338.
[26] Z. Liu, Q. Xu, Y. Zhu, N. Xu, H. Chu, J. Wang, Insight into the principles of photothermal superhydrophobic coatings, recent advances in anti-/de-icing, frontier applications and future challenges, Adv. Colloid Interface Sci. 352 (2026) 103830.
[27] D. Seo, S. Oh, B. Moon, H. Kim, J. Kim, C. Lee, Y. Nam, Influence of lubricant-mediated droplet coalescence on frosting delay on lubricant impregnated surfaces, Int. J. Heat Mass Transf. 128 (2019) 217–228.
[28] J. Jiang, Q. Sheng, G.H. Tang, M.Y. Yang, L. Guo, Anti-icing propagation and icephobicity of slippery liquid-infused porous surface for condensation frosting, Int. J. Heat Mass Transf. 190 (2022) 122730.
[29] M.J. Hoque, S. Sett, X. Yan, D. Liu, K.F. Rabbi, H. Qiu, M. Qureshi, G. Barac, L. Bolton, N. Miljkovic, Life span of slippery lubricant infused surfaces, ACS Appl. Mater. Interfaces 14 (3) (2022) 4598–4611.
[30] D. Ghaddar, K. Boyina, K. Chettiar, S. Wang, N. Miljkovic, Effect of aluminum heat exchanger surface wettability on condensation heat transfer and water harvesting performance, Int. J. Heat Mass Transf. 243 (2025) 126835.
[31] W.S.Y. Wong, K.I. Hegner, V. Donadei, L. Hauer, A. Naga, D. Vollmer, Capillary balancing: designing frost-resistant lubricant-infused surfaces, Nano Lett. 20 (12) (2020) 8508–8515.
[32] L. Wang, T.J. McCarthy, Covalently attached liquids: instant omniphobic surfaces with unprecedented repellency, Angew. Chem. Int. Ed. 55 (1) (2016) 244–248.
[33] L. Chen, S. Huang, R.H.A. Ras, X. Tian, Omniphobic liquid-like surfaces, Nat. Rev. Chem. 7 (2) (2023) 123–137.
[34] J.V. Buddingh, A. Hozumi, G. Liu, Liquid and liquid-like surfaces/coatings that readily slide fluids, Prog. Polym. Sci. 123 (2021) 101468.
[35] B. Khatir, Z. Azimi Dijvejin, P. Serles, T. Filleter, K. Golovin, Molecularly capped omniphobic polydimethylsiloxane brushes with ultra-fast contact line dynamics, Small 19 (38) (2023) e2301142.
[36] G. McHale, N. Gao, G.G. Wells, H. Barrio-Zhang, R. Ledesma-Aguilar, Friction coefficients for droplets on solids: the liquid-solid amontons' laws, Langmuir 38 (14) (2022) 4425–4433.
[37] L. Zhang, Z. Guo, J. Sarma, X. Dai, Passive removal of highly wetting liquids and ice on quasi-liquid surfaces, ACS Appl. Mater. Interfaces 12 (17) (2020) 20084–20095.
[38] H. Zhao, S. Khodakarami, C.A. Deshpande, J. Ma, Q. Wu, S. Sett, N. Miljkovic, Scalable slippery omniphobic covalently attached liquid coatings for flow fouling reduction, ACS Appl. Mater. Interfaces 13 (32) (2021) 38666–38679.
[39] M. Ghasemlou, C. Stewart, S. Jafarzadeh, M. Dokouhaki, M. Mathesh, M. Naebe, C. J. Barrow, Self-lubricated, liquid-like omniphobic polymer brushes: advances and strategies for enhanced fluid and solid control, Prog. Polym. Sci. 162 (2025) 101933.
[40] I.J. Gresham, C. Neto, Advances and challenges in slippery covalently-attached liquid surfaces, Adv. Colloid Interface Sci. 315 (2023) 102906.
[41] J. Sarma, L. Zhang, Z. Guo, X. Dai, Sustainable icephobicity on durable quasi-liquid surface, Chem. Eng. J. 431 (2022) 133475.
[42] C. Haensch, S. Hoeppener, U.S. Schubert, Chemical modification of self-assembled silane based monolayers by surface reactions, Chem. Soc. Rev. 39 (6) (2010) 2323–2334.

[43] S. Wooh, N. Encinas, D. Vollmer, H.J. Butt, Stable hydrophobic metal-oxide photocatalysts via grafting polydimethylsiloxane brush, Adv. Mater. 29 (16) (2017) 1604637.
[44] S. Yang, F. Chu, V. Ganesan, P. Faghihi, D. Ghaddar, W. Zhang, J. Liu, J.B. Yang, A. Huang, K. Boyina, K. Chettiar, S. Dewanjee, S. Aflatounian, R. Khan, P.V. Braun, J. Feng, D. Poulikakos, N. Miljkovic, Growth and control of suspended ice bridges during sessile droplet freezing, Nat. Phys. (22, 2026, 1136–1143).
[45] K. Alshamani, Equations for physical properties of automotive coolants, in: SAE Technical Papers, 2003.
[46] D. Ghaddar, K. Chettiar, S.A. Haider, J. Liu, K. Boyina, N. Miljkovic, Experimental study of frost formation and various defrosting techniques on a microchannel evaporator in a real reversible air source heat pump system, in: International Refrigeration and Air Conditioning Conference, 2024, p. Paper 2512.
[47] A. Standard, Performance rating of unitary air-conditioning & air-source heat pump equipment, in: AHRI Standard, 2008, p. 240.
[48] P. Wang, L. Tong, R. Wang, A. Chen, W. Fang, K. Yue, T. Sun, Y. Yang, Improved performances of lithium-ion batteries using intercalated a-Si-Ag thin film layers as electrodes, RSC Adv. 8 (72) (2018) 41404–41414.
[49] J. Liu, Y. Sun, X. Zhou, X. Li, M. Kappl, W. Steffen, H.J. Butt, One-step synthesis of a durable and liquid-repellent poly(dimethylsiloxane) coating, Adv. Mater. 33 (23) (2021) e2100237.
[50] F. Liu, G. Ghigliotti, J.J. Feng, C.H. Chen, Self-propelled jumping upon drop coalescence on leidenfrost surfaces, J. Fluid Mech. 752 (2014) 22–38.
[51] J. Jiang, J. Gao, H. Zhang, W. He, J. Zhang, D. Daniel, X. Yao, Directional pumping of water and oil microdroplets on slippery surface, Proc. Natl. Acad. Sci. USA 116 (7) (2019) 2482–2487.
[52] X. Zhang, L. Sun, Y. Wang, F. Bian, Y. Wang, Y. Zhao, Multibioinspired slippery surfaces with wettable bump arrays for droplets pumping, Proc. Natl. Acad. Sci. USA 116 (42) (2019) 20863–20868.
[53] J. Sun, P.B. Weisensee, Microdroplet self-propulsion during dropwise condensation on lubricant-infused surfaces, Soft Matter 15 (24) (2019) 4808–4817.
[54] J. Sun, P.B. Weisensee, Marangoni-induced reversal of meniscus-climbing microdroplets, Soft Matter 19 (4) (2023) 625–633.
[55] J.J. Mitchell, F.F. Coleman, Hydrocarbon ion appearance potentials, J. Chem. Phys. 17 (1) (1949) 44–55.
[56] J.B. Boreyko, R.R. Hansen, K.R. Murphy, S. Nath, S.T. Retterer, C.P. Collier, Controlling condensation and frost growth with chemical micropatterns, Sci. Rep. 6 (2016) 19131.
[57] S. Nath, S.F. Ahmadi, J.B. Boreyko, A review of condensation frosting, Nanoscale Microsc. Thermophys. Eng. 21 (2) (2016) 81–101.
[58] S. Nath, J.B. Boreyko, On localized vapor pressure gradients governing condensation and frost phenomena, Langmuir 32 (33) (2016) 8350–8365.
[59] S. Jung, M.K. Tiwari, D. Poulikakos, Frost halos from supercooled water droplets, Proc. Natl. Acad. Sci. USA 109 (40) (2012) 16073–16078.
[60] S. Zhen, H. Feng, S. Lin, Y. Jin, Z. Li, X. Deng, E. Bonaccurso, L. Chen, Condensate halos in condensation frosting, Adv. Sci. 12 (14) (2025) e2410657.
[61] S. Yang, J. Yang, D. Yoo, N. Wszolek, Q. Huang, I. Lee, R. Khan, K. Chettiar, A. Ahmed, C. Zhang, A. Riahi, N. Miljkovic, Comprehensive analysis of scalable anti-frosting and anti-corrosion heat exchanger coatings, Int. J. Heat Mass Transf. 271 (2026) 129453.
[62] H. Xing, H. Jin, C. Wang, X. Liu, Experimental study on crystal deposition mechanism of ammonium chloride particles on the surface of heat exchange tube, Powder Technol. 421 (2023) 118440.
[63] Y. He, D. Walsh, C. Shi, Fluoropolymer composite coating for condensing heat exchangers: characterization of the mechanical, tribological and thermal properties, Appl. Therm. Eng. 91 (2015) 387–398.
[64] A.C. Scott, R.A. Woods, J.F. Harris, Accelerated corrosion test methods for evaluating external corrosion resistance of vacuum brazed aluminum heat exchangers, in: SAE Technical Papers, 1991.
[65] L.T. Li, W. Wang, Y.Y. Sun, Y.C. Feng, W.P. Lu, J.H. Zhu, Y.J. Ge, Investigation of defrosting water retention on the surface of evaporator impacting the performance of air source heat pump during periodic frosting–defrosting cycles, Appl. Energy 135 (2014) 98–107.
[66] B. Xu, Q. Han, J. Chen, F. Li, N. Wang, D. Li, X. Pan, Experimental investigation of frost and defrost performance of microchannel heat exchangers for heat pump systems, Appl. Energy 103 (2013) 180–188.
[67] L. Pu, R. Liu, H. Huang, S. Zhang, Z. Qi, W. Xu, J. Zhou, Experimental study of cyclic frosting and defrosting on microchannel heat exchangers with different coatings, Energy Build. 226 (2020) 110382.
[68] V. Donadei, H. Koivuluoto, E. Sarlin, H. Niemelä-Anttonen, T. Varis, P. Vuoristo, The effect of mechanical and thermal stresses on the performance of lubricated icephobic coatings during cyclic icing/deicing tests, Prog. Org. Coat. 163 (2022) 106614.
[69] M.J. Hoque, X. Yan, H. Qiu, Y. Qin, X. Du, J. Stermer, N. Miljkovic, Durability and degradation mechanisms of antifrosting surfaces, ACS Appl. Mater. Interfaces 15 (10) (2023) 13711–13723.
[70] W. Ma, A.A. Sergeev, M.B. Asif, Y. Pan, H. Wang, K. Li, A. Safari, J. Yang, B. Huang, K.S. Wong, Y. Li, X. Yan, S. Yao, Robust all-day frostphobic surfaces, ACS Appl. Mater. Interfaces 16 (33) (2024) 44174–44185.